1 # Genetically Encoded and Modular SubCellular Organelle Probes (GEM-

2 SCOPe) reveal lysosomal and mitochondrial dysfunction driven by *PRKN*

3 knockout

4 Camille Goldman[1-5], Tatyana Kareva[1-5], Lily Sarrafha[1-5], Braxton R. Schuldt[1-5], Abhishek

5 Sahasrabudhe[1-3], Tim Ahfeldt[1-5] **, Joel W. Blanchard[1-6] *

6   1. Icahn School of Medicine, Mount Sinai, New York, NY, USA

7   2. Nash Family Department of Neuroscience, Mount Sinai, New York, NY, USA

8   3. Friedman Brain Institute, Mount Sinai, New York, NY, USA

9   4. Ronald M. Loeb Center for Alzheimer's Disease, Mount Sinai, New York, NY USA

10   5. Black Family Stem Cell Institute, Mount Sinai, New York, NY, USA

11   6. Lead Contact

12   * Corresponding author

13   ** 2nd corresponding author

14   Correspondence: joel.blanchard@mssm.edu

15   Correspondence: ahfeldt@gmail.com

16 Summary

17 Cellular processes including lysosomal and mitochondrial dysfunction are implicated in the

18 development of many diseases. Quantitative visualization of mitochondria and lysosoesl is crucial

19 to understand how these organelles are dysregulated during disease. To address a gap in live-

20 imaging tools, we developed GEM-SCOPe (Genetically Encoded and Modular SubCellular

21 Organelle Probes), a modular toolbox of fluorescent markers designed to inform on localization,

22 distribution, turnover, and oxidative stress of specific organelles. We expressed GEM-SCOPe in

23 differentiated astrocytes and neurons from a human pluripotent stem cell *PRKN*-knockout model

24 of Parkinson's disease and identified disease-associated changes in proliferation, lysosomal

25 distribution, mitochondrial transport and turnover, and reactive oxygen species. We demonstrate

26 GEM-SCOPe is a powerful panel that provide critical insight into the subcellular mechanisms

27 underlying Parkinson's disease in human cells. GEM-SCOPe can be expanded upon and applied

28 to a diversity of cellular models to glean an understanding of the mechanisms that promote

29 disease onset and progression.

Keywords

Live-cell imaging, induced pluripotent stem cells, Parkinson's Disease, astrocytes, PRKN

Introduction

Parkinson's Disease (PD) is a common neurodegenerative disease that robs individuals of their motor and cognitive functions, affecting over 10 million people worldwide and with an estimated 90,000 new diagnoses in the United States each year[1]. PD is clinically characterized by bradykinesia, resting tremor, rigidity, and postural instability[2-5] and pathologically characterized by the loss of dopaminergic neurons in the substantia nigra pars compacta and buildup of intracellular deposits of α-synuclein into insoluble protein aggregates called Lewy Bodies[2,6-8]. From the first pathological descriptions of PD in the mid-20th century, advancements in many fields, including histology, genetics, cell biology, and neurology enabled insight into many aspects of the disease, from determining genetic and environmental risk factors and mapping disease progression to identifying pathways and proteins to target therapeutically. Despite great progress, there is still incomplete understanding of the cellular dysfunction that precedes and contributes to chronic neuronal death.

This limited advancement arises in part due to the absence of tools used to track molecular and cellular changes in real-time throughout disease progression. Studies on human post-mortem brain tissue are largely representative of end-stage disease states, making it difficult to dissect which phenotypes are a primary, causative effect and which phenotypes are a secondary response[9]. Mouse models offer more opportunities to study multiple time points throughout disease progression as motor and cognitive symptoms can be monitored over time. However, targeting specific cell types in mice remains technically challenging and time-consuming.

53   Emerging technologies such as the miniscope allow continuous monitoring of fluorescence-based

54   readouts on a cellular level in live mouse and rat brains[10-12]. However, the type of readout from

55   the miniscope has been restricted to neuronal activity from fluorescent calcium sensors and

56   resolution along the z-axis remains a limiting factor in analyzing deeper cortical tissue.

57   Regardless of such technologies, current genetic rodent models of PD fail to completely

58   recapitulate human disease and lack key pathological hallmarks. Drug-induced models can

59   recapitulate late-stage disease phenotypes and behaviors, but due to their acute onset, are

60   inadequate to study the gradual accumulation of cellular dysfunction that precedes clinical

61   presentation[13,14]. Advancements in induced pluripotent stem cell (iPSC) differentiation and

62   CRISPR/Cas9 genome editing have led to the emergence of genetic cellular models of PD[15-18].

63   These models enable researchers to study the effects of genetic and environmental factors on

64   specific human cell populations relevant to PD.

65   Cellular models of PD provide an exciting opportunity to study subcellular changes and responses

66   to stress or treatment in live cells. Cells can be genetically engineered to express fluorescent

67   proteins that can then be visualized by microscopy in live cells. The applicability of GFP as a

68   reporter gene was immediately appreciated after its identification and isolation in 1962[19]. Since

69   then, hundreds of fluorophores have been developed by introducing mutations to naturally

70   occurring fluorophores isolated from sea anemones and jellyfish to modulate fluorescence

71   intensity, half-life, and excitation/emission spectra[20]. Additional fluorophores have been

72   developed as biosensors, by fluorescing or changing fluorescence emission in the presence of a

73   certain ligand or under specific cellular conditions[20-25]. Cells can express these fluorophores with

74   virtually limitless possibilities with regards to subcellular localization, cell-type specific expression,

75   and temporally controlled expression. Genetically encoded fluorescent proteins can be used to

76   follow a population of cells as they change due to aging, genetics, or environmental stressors and

77   stimuli.

78   PD has a complex genetic architecture underlying the disease. Over 90% of PD cases are

79   idiopathic; over 90 genetic risk loci have been identified by GWAS, but any of those individual

80   variants confer little risk on their own[26]. The remaining 10% of PD cases can be linked to highly

81   penetrant mutations in a handful of genes. While extremely rare, studying the function of these

82   genes and their impact on cellular processes sheds light on the fundamental pathways that drive

83   PD pathogenesis. Here, we focus on the *PRKN* gene. Autosomal recessive loss of function

84   mutations in *PRKN* are the most frequent known genetic cause of early onset cases of PD,

85   accounting for about 15% of PD cases with onset before the age of 50[27-30]. *PRKN* encodes for

86   the protein PRKN, an E3 ubiquitin ligase associated with mitochondria. PRKN directs the

87   ubiquitination of outer mitochondrial membrane proteins on damaged mitochondria, targeting

88   them for degradation via the autophagy-lysosomal pathway (mitophagy)[31-33]. While the function

89   of PRKN is well understood, it is still unclear how loss of PRKN function leads to the gradual

90   disease progression of early onset PD. It is believed that neurodegeneration can begin over 20

91   years before clinical onset, with a prolonged prodromal phase associated with several non-motor

92   symptoms. Thus, it is crucial to study models of early disease to understand what cellular

93   disturbances in the prodromal phase culminate in neurodegeneration.

94   Here, we present GEM-SCOPe (**G**enetically **E**ncoded and **M**odular **S**ub**C**ellular **O**rganelle

95   **P**robes), an expandable panel of genetically encoded reporters to track and quantify the

96   subcellular phenotypes in live cells. We developed a library of constructs that localize specifically

97   to the nucleus, mitochondria, and lysosomes and included fluorophores with a variety of emission

98   spectra or biosensor capabilities. All the lentiviral constructs were developed in the same

99   backbone vector to be modular, enabling any component, be it promotor, localization signal,

100   fluorophore, or antibiotic resistance, to be easily removed or replaced. We validated the

101   fluorophores with live-imaging of human induced pluripotent stem cell (hiPSC)-derived midbrain

102   astrocytes employing existing chemical dyes and chemical perturbations. We then applied GEM-

103   SCOPe to hiPSC-derived astrocytes and neurons from a *PRKN*-knockout model of PD[15]. This

104   revealed previously unseen changes in cellular proliferation, lysosomal distribution, mitochondrial

105   motility and turnover, and reactive oxygen species production. Our results demonstrate the

106   widespread utility of GEM-SCOPe to study a variety of translationally important subcellular

107   changes affected during PD. The modular, combinatorial flexibility of GEM-SCOPe can be

108   adapted to investigate any disease, and, therefore, it is a critical new resource that can be broadly

109   applied in neurodegenerative research and beyond.

110

Results

Building a modular toolbox for the subcellular localization of genetically encoded fluorophores

114   We developed GEM-SCOPe for live-cell imaging of subcellular organelle dynamics. We aimed to

115   produce a system that is highly modular to easily customize the expression, localization,

116   fluorescence, and selection for any given experimental need. We started with the FUW

117   backbone[34], a 3rd generation lentivirus backbone with a ubiquitin C promoter for high, ubiquitous

118   expression of the transgene across cell types[34,35] and a woodchuck hepatitis virus post-

119   transcriptional regulatory element (WPRE) for improved lentiviral expression[34,36,37]. The designed

120   lentiviral constructs contain four components: promoter, localization sequence, fluorophore, and

121   antibiotic resistance (**Fig. 1A**). The content of these four components can be mixed and matched

122   to generate a library of lentiviral constructs to fit a diverse field of experimental needs. To generate

123   constructs *de novo*, components were combined and inserted into the plasmid via Gibson

124   assembly (**Fig. 1B, top**). Restriction sites were kept between each domain, so each component

125   or group of components could be excised via restriction digest and replaced with a different

126 component, either by restriction site cloning or Gibson assembly (**Fig. 1B, bottom**). Thus, each

127 component of the lentiviral plasmid can be removed or replaced to accommodate features such

128 as cell-type specificity with cell-type specific promoters, alternative subcellular localization, and

129 unique fluorophores.

130 The FUW backbone has a ubiquitin C promoter, but this can be replaced with lineage or cell-type-

131 specific promoters for selective expression in specific cell types or with drug-inducible promoters

132 to temporally control when the construct is transcribed (**Fig. S1A**). Subcellular localization is

133 determined by including the whole or partial coding sequence of a peptide with a known and

134 specific subcellular localization. This domain can be omitted to produce a fluorophore expressed

135 in the cytoplasm. The fluorophore component of the construct offers the most flexibility, from basic

136 fluorescent proteins to more complex fluorophores that change fluorescent excitation and/or

137 emission wavelength with time or environment. All plasmids generated for GEM-SCOPe have

138 been deposited to Addgene(**Table S1**).

139 We developed GEM-SCOPe constructs to localize fluorophores to the cytoplasm (no tag), nucleus

140 (H2B-tag), mitochondria (COX8A-tag), and lysosome (LAMP1-tag) (**Fig. 1C**). Fluorophore

141 localization was validated using commercially available live cellular dyes. Nuclear localization was

142 achieved by fusing fluorophores to the C-terminus of histone 2B (H2B). H2B is an integral

143 chromatin protein that is found in all cells and is localized specifically to the nucleus[38,39]. H2B

144 fused to mTagBFP2, a blue fluorophore, (H2B-mTagBFP2) co-localizes with DRAQ5, a far-red

145 live-cell nuclear dye[40] (**Fig. 1C, top**; Mander's coefficient > 0.99±0.0001). In addition to the

146 mTagBFP2 construct, we also developed lentiviral plasmids with H2B fused to Emerald (green;

147 H2B-Emerald) and mCherry (red; H2B-mCherry) (**Fig. 1A, S1B**).

148 To localize fluorophores to the lysosome, we utilized the N-terminal peptide sequence of

149 lysosomal-associated membrane protein 1 (LAMP1), a major component of lysosomal

150 membranes that plays a key role in lysosomal biogenesis and homeostasis. The N-terminus of

151 LAMP1 fused to mCherry (LAMP1-mCherry) co-localizes with LysoTracker (Thermo Scientific)

152 (**Fig. 1C, middle**; Mander's coefficient = 0.92±0.03). LysoTracker is a fluorophore that is partially

153 protonated at neutral pH and can readily cross membranes; once protonated it can no longer

154 diffuse so the fluorescent signal gets trapped in acidic compartments, including, but not limited to,

155 the lysosome[41,42]. Overexpression of LAMP1 is associated with numerous cancers and cancer

156 metastasis[43-46]. By only using a partial sequence of LAMP1 and not the full peptide sequence, we

157 are able to target the fluorophore specifically to the lysosome without increasing the expression

158 of endogenous LAMP1 (**Fig. S1C**). We also developed lentiviral plasmids with the LAMP1

159 targeting sequence fused to Emerald (green; LAMP1-Emerald; **Fig. 1A, 1D**).

160 Finally, mitochondrial localization was achieved using the mitochondrial targeting sequence of

161 COX8A. COX8A is a nuclear-encoded subunit of cytochrome-c oxidase (Complex IV) in the

162 electron transport chain[47,48]. The first 25 amino acid residues of the COX8A peptide sequence

163 target the peptide to the mitochondrial inner membrane and are widely used to specifically localize

164 proteins and fluorophores to the mitochondria[49-51]. To confirm mitochondrial specificity of COX8A-

165 Emerald we compared localization with MitoTracker (Thermo Scientific), a dye that accumulates

166 in the mitochondria due to the negative membrane potential of the inner mitochondrial

167 membrane[41,52]. The mitochondrial targeting sequence fused to an Emerald fluorophore (COX8A-

168 Emerald) exhibited significant co-localization with MitoTracker (**Fig. 1C, bottom**; Mander's

169 coefficient = 0.97±0.003). We developed lentiviral plasmids with the COX8A targeting sequence

170 fused to mCherry (red; COX8A-mCherry; **Fig. 1A, 1D**), Timer (green/red; COX8A-Timer; **Fig. 1A,**

171 **Fig. 5**), and Lemon (cyan/yellow; COX8A-Lemon; **Fig. 1A, Fig. S2**).

172 Once the localization strategies were finalized, we swapped out the fluorophores with different

173 fluorescent proteins that are excited and emitted at alternative wavelengths. Mixing localization

174 sequences and fluorophores with unique emission spectra allows simultaneous imaging of

175 multiple sub-cellular processes in the same cells such as mitochondrial network and lysosomal

176 distribution (**Fig. 1D**). Utilizing a combination of subcellular localization and diverse fluorophores,

177 we developed GEM-SCOPe, a fluorescent, live-cell imaging toolbox of lentiviral constructs that

178 were systematically validated to quantify cellular proliferation, lysosomal distribution, and

179 mitochondrial dynamics in human Parkinson's disease astrocytes.

180

H2B-fused fluorophores offer improvements for efficiently labelling nuclei for multi-day live-cell assays

183 Quantification of cellular phenotypes by fluorescence microscopy is dependent on normalization

184 to total cell number. This is often accomplished by counting the number of nuclei. A few fluorescent

185 dyes that can cross the cellular and nuclear membranes of live cells and bind specifically to DNA

186 are commercially available. While efficient for short-term and end-point assays, such dyes

187 intercalate in DNA and therefore have cytotoxic and mutagenic effects[53,54]. Furthermore, nuclear

188 dyes do not remain contained within the nuclear compartment, and their signal leaches into the

189 cytoplasm in just a few hours after exposing the cells. The cytotoxicity and loss of precise labeling

190 over time render these dyes less useful for long-term microscopy or cell-tracking experiments. To

191 address these concerns, we developed lentiviral constructs expressing nuclear-localized

192 fluorophores by fusing the nucleus-specific histone protein, H2B, with either mTagBFP2, Emerald,

193 or mCherry (**Fig. 1C, 2A**). Human induced pluripotent stem-cell (hiPSC)-derived astrocytes

194 transfected with H2B-mTagBFP2 were co-stained with DRAQ5, a far-red DNA-stain for live cells.

195 The localization of the two nuclear signals was compared 1 hours and 24 hours after the addition

196 of DRAQ5. Immediately after adding DRAQ5, there was no difference between the DRAQ5 stain

197 and the H2B-mTagBFP2 (2-way ANOVA with Tukey's HSD; adj-p = 0.83) (**Fig. 2B, C**). Over the

198 experimental period, the DRAQ5 signal spread significantly ($26\pm5\%$ extranuclear; adj-p < 0.0001),

199 while the extranuclear H2B-mTagBFP2 signal did not significantly change (adj-p = 0.99) (**Fig. 2B,**

200   **C**). While the human eye can still readily distinguish the nucleus from the extranuclear stain in the

201   DRAQ5 images, image analysis programs that rely on grey values for segmentation often fail to

202   correctly differentiate the true nuclear signal from the extranuclear signal. Thus, lentiviral

203   constructs expressing nuclear-localized fluorophores, such as the demonstrated H2B-

204   mTagBFP2, can provide better alternatives for long-term live-imaging experiments with multiple

205   time points.

206

H2B-fused fluorophores reveal increased cellular proliferation in PRKN knockout astrocytes

209   While dopaminergic neuron death is the predominant cellular outcome in Parkinson's Disease

210   (PD), other cell types in the brain may change cell cycle regulation under neurotoxic conditions.

211   Tracking cell numbers to monitor proliferation, senescence, or death in vitro can help researchers

212   understand how different cell populations are responding to neurotoxic stress or potential

213   therapeutic strategies.

214   First, we validated that our nuclear-localized construct, H2B-Emerald, could be used to track

215   cellular proliferation. The proliferation of H2B-Emerald transduced hiPSC-derived astrocytes was

216   induced using fetal bovine serum (FBS) or blocked by inhibiting the proteasome with MG-132.

217   Astrocyte proliferation was measured by changes in the number of H2B-Emerald nuclei. As

218   expected, the astrocytes treated with FBS proliferated twice as rapidly as the untreated astrocytes

219   over 48 hours (2-way ANOVA with Tukey's HSD, p-adj = 0.005, **Fig. S3**), while the astrocytes

220   treated with MG-132 did not significantly proliferate over the same period (adj-p = 0.08, **Fig. S3**).

221   Thus, the GEM-SCOPe H2B-fluorophore fusion proteins can be used to track cellular proliferation

222   over multiple days in live cell cultures.

223   To examine the effect of loss of *PRKN* on astrocyte proliferation, we transduced wild-type

224   (*PRKN*^{+/+}) astrocytes with H2B-Emerald and isogenic *PRKN* knockout (*PRKN*^{-/-}) astrocytes with

225   H2B-mCherry (**Fig. 2D**). Leveraging the modularity of GEM-SCOPe, we were able to mix the two

226   astrocyte populations together and track their proliferation simultaneously. Over 48 hours, the

227   *PRKN*^{-/-} population increased significantly (2-way ANOVA with Tukey's HSD, p-adj = 0.03; **Fig.**

228   **2E, F**) while the *PRKN*^{+/+} population did not proliferate in the same period (2-way ANOVA with

229   Tukey's HSD, p-adj = 0.4; **Fig. 2E, F**). These results contradict mouse studies that found that

230   PRKN-null mice had decreased astroglia proliferation[55]. However, PRKN has also been described

231   as a tumor suppressor, with loss of function mutations arising in a variety of cancers, including

232   glioblastomas[56-58]. Studies on PRKN in the context of cancer find that cancer regulates the

233   degradation of cyclins and cyclin-dependent kinases involved in the G1/S transition, thus

234   promoting continued proliferation[57,59,60]. It has been hypothesized that the outcome of loss of

235   function PRKN mutations are highly cell-context dependent; the increased half-life of cyclins leads

236   to cancer in mitotically competent cells while the same cyclins promote apoptosis upon cell cycle

237   reentry in post-mitotic neurons[57,61-64]. Our findings highlight the importance of studying disease-

238   relevant human cells to capture the intricacies and nuances specific to the human brain that could

239   contribute to PD.

240

LAMP1-localized fluorophores reveal changes in lysosomal

distribution in response to chemical and genetic stressors

243   Lysosomal dysfunction is widely implicated in PD and other forms of neurodegeneration. Several

244   PD-risk and familial genes are involved in the autophagy-lysosomal-endosomal pathway[65-67], and

245   many hallmarks of lysosomal dysfunction associated with familial PD are present in idiopathic PD

246   [66,68,69]. Disruption to the autophagy-lysosomal-endosomal pathway is of broad importance in PD

247 and there is a crucial need to study lysosomal function and dysfunction in the context of PD

248 pathogenesis. As described above, we fused the N-terminus of LAMP1 to a fluorophore (Emerald

249 or mCherry) to specifically target the fluorescent signal to the lysosome (**Fig. 1C, 3A**). To validate

250 the GEM-SCOPe LAMP1-mCherry signal responds to lysosomal stress, hiPSC-derived

251 astrocytes transduced with LAMP1-mCherry lentivirus were exposed to bafilomycinA1 (BafA1) for

252 15 hours. BafA1 inhibits lysosomal proton pump V-ATPases, which blocks autophagosome-

253 lysosome fusion and lysosomal acidification, impairing lysosomal function [70,71]. hiPSC-derived

254 astrocytes were simultaneously transduced with a non-localized Emerald fluorophore lentivirus,

255 to provide a cell body marker. We used CellProfiler [72] to evaluate the lysosomal number, size, and

256 distribution within each cell. Compared to vehicle (DMSO) treatment, treatment with BafA1

257 increased the number of LAMP1-mCherry vesicles (unpaired t-test, p = 0.04; **Fig. 3B, C**), but did

258 not affect lysosome size (unpaired t-test, p = 0.16, **Fig. 3B, C**). Treatment with BafA1 altered the

259 distribution of lysosomes within the astrocytes. Astrocytes treated with BafA1 had a more

260 dispersed distribution of LAMP1-mCherry signal, with only 41±4% concentrated in the perinuclear

261 area, in contrast to 65±8% in vehicle-treated astrocytes (unpaired t-test, p = 0.002; **Fig. 3B, C**).

262 Perinuclear and juxtanuclear lysosomes have been posited to be more acidic than peripheral

263 lysosomes[73]. Lysosomal distribution can also be affected by cytosolic pH, with acidification

264 promoting the spreading of lysosomes away from the nucleus[74-76]. Since BafA1 inhibits V-

265 ATPases responsible for establishing and maintaining lysosomal pH, the redistribution of

266 lysosomes away from the nucleus upon BafA1 treatment might reflect a change in lysosomal or

267 cytosolic pH, and therefore lysosomal function, in the treated astrocytes.

268 In addition to its role in ubiquitinating damaged mitochondria for degradation via the autophagy-

269 lysosomal pathway[31-33], PRKN has been shown to regulate endosome organization[77] and

270 mitochondria-lysosome contact sites. Although it has been reported that *PRKN* knockout in

271 hiPSC-derived dopaminergic neurons leads to an increase in lysosome number and size

272 compared to isogenic, wild-type dopaminergic neurons[78], the effect of *PRKN* knockout on

273 lysosomes on human astrocytes is largely unknown. Due to PRKN's role in regulating the

274 autophagy-lysosomal pathway, we hypothesized *PRKN^{-/-}* in human astrocytes would disrupt

275 lysosomal dynamics. To test this hypothesis, we applied the same CellProfiler analysis on

276 *PRKN^{+/+}* and *PRKN^{-/-}* hiPSC-derived astrocytes transduced with GEM-SCOPe Emerald and

277 LAMP1-mCherry lentivirus. *PRKN^{-/-}* astrocytes had half as many LAMP1-mCherry vesicles per

278 cell compared to *PRKN^{+/+}* astrocytes (unpaired t-test, p = 0.003, **Fig. 3D, E**). Additionally, the

279 *PRKN^{-/-}* lysosomes were smaller than the *PRKN^{+/+}* lysosomes (unpaired t-test, p = 0.055, **Fig. 3D,**

280 **E**). Finally, the *PRKN^{-/-}* astrocytes had a decrease in perinuclear LAMP1-mCherry, with only

281 38±4% of LAMP1-mCherry signal located in the perinuclear area, compared to 45±3% in

282 *PRKN^{+/+}* (unpaired t-test, p = 0.005, **Fig. 3D, E**). Our results utilizing our GEM-SCOPe LAMP1-

283 mCherry fluorophore suggest that lysosomal distribution in astrocytes is altered upon loss of

284 *PRKN* and further studies to examine lysosomal content and activity are needed to understand

285 the implications and how this could differ from observations in other cell types.

286

287 **Mitochondria-localized fluorophores capture mitochondrial**

288 **fragmentation and alterations in mitochondrial trafficking**

289 **along PRKN knockout dopaminergic neuron axons**

290 Much like lysosomal dysfunction, mitochondrial dysfunction is implicated in PD and

291 neurodegeneration. Therefore, monitoring mitochondrial network dynamics in response to stimuli

292 and stress is important in understanding neurodegenerative diseases. As described above, we

293 fused the N-terminus of the mitochondrial protein COX8A to a fluorophore (Emerald or mCherry)

294 to localize the fluorophore specifically to the mitochondria (**Fig. 1C, 4A**). To validate that GEM-

295   SCOPe COX8A localized fluorophores reflect changes to mitochondrial morphology, we induced

296   mitochondrial stress by treating hiPSC-derived astrocytes transduced with the COX8A-mEmerald

297   lentivirus with 2μM oligomycin for 4 hours. Mitochondrial stress induces fragmentation of the

298   mitochondrial network, which facilitates mitophagy, but also decreases mitochondrial network

299   respiratory capacity[79,80]. Oligomycin, an inhibitor of ATP synthase, is a known inducer of

300   mitochondrial fragmentation. Treatment with oligomycin induced mitochondrial fragmentation

301   when compared to vehicle-treated astrocytes. The average area of mitochondria was reduced

302   from 1.04 μm^2 in vehicle-treated astrocytes to 0.8 μm^2 in oligomycin-treated astrocytes (1-way

303   ANOVA with Dunett's Test, p-adj = 0.0002; **Fig. 4B, C left)**, and average branch length was

304   reduced from 1.28 μm in vehicle-treated astrocytes to 0.9 μm in oligomycin treated astrocytes (1-

305   way ANOVA with Dunett's Test, p-adj < 0.0001; **Fig. 4B, C middle)**, as expected from a more

306   fragmented mitochondrial network. The aspect ratio is the ratio of the mitochondrial length to

307   width. An aspect ratio of 1 indicates a perfect circle, while larger aspect ratios indicate longer and

308   narrower shapes. The mean aspect ratio decreased from 2.52 in vehicle-treated astrocytes to

309   2.14 in oligomycin-treated astrocytes (1-way ANOVA with Dunett's Test, p-adj < 0.0001; **Fig. 4B,**

310   **C right**), another indicator that mitochondria are fragmenting upon oligomycin treatment. Metrics

311   of mitochondrial network fragmentation (mitochondrial area, branch length, and aspect ratio) are

312   all affected in a dose-dependent manner, with increasing concentrations of oligomycin having

313   increasingly more severe effects on mitochondrial network fragmentation (**Fig. S4**).

314   The transport of mitochondria along neuronal axons is critical for proper synaptic function and

315   neurotransmitter release. We hypothesized *PRKN*^{-/-} may impair axonal mitochondrial transport.

316   To investigate this hypothesis, we transduced wild-type (*PRKN*^{+/+}) and *PRKN* knock-out (*PRKN*^{-/-}

317   ) hiPSC-derived midbrain organoids with COX8A-mEmerald. To facilitate imaging of axonal

318   mitochondrial transport, we generated radial axonal arbors by splatting organoids onto the surface

319   of a plate and allowing the axons to grow out[81]. On day 164 of organoid differentiation, fluorescent

320 mitochondria were imaged at high magnification over several minutes to monitor the movement

321 of mitochondria along these axons (**Fig. 4D; Video S1**). In the anterograde direction (moving

322 away from the soma), $PRKN^{-/-}$ mitochondria moved only 20% of the distance covered by $PRKN^{+/+}$

323 mitochondria (Welch's t-test, p < 0.0001, **Fig. 4E left**) and took 50% longer (unpaired t-test, p =

324 0.005; **Fig. 4E right**). Retrograde-moving mitochondria moved the same distance (unpaired t-

325 test, p = 0.59, **Fig. 4F left)** but the $PRKN^{-/-}$ mitochondria moved for 150% longer compared to the

326 $PRKN^{+/+}$ mitochondria (Welch's t-test, p = 0.02; **Fig. 4F right**). PRKN has previously been

327 implicated in mitochondrial transport due to its ubiquitination of mitochondrial motor adaptor

328 complexes[82]. Our results demonstrate that PRKN loss of function impairs mitochondrial trafficking

329 in human neurons, likely reducing the delivery of functional mitochondria synaptic extremities and

330 ultimately compromising neuronal function.

Dynamic fluorophores measure deficiencies in mitochondrial turnover and glutathione reduction potential in PRKN-knockout astrocytes

334 We demonstrated the utility of single excitation and emission wavelengths to discern phenotypes

335 regarding cellular and subcellular dynamics. Numerous groups have developed fluorophores that

336 change emission wavelengths under certain conditions or circumstances. We introduced several

337 multi-emission fluorophores into GEM-SCOPe to enable quantification of organelle turnover,

338 acidification, and oxidation, in addition to the localization information described with the previous

339 fluorophores.

340 Fluorescent Timer is a mutated dsRed protein that irreversibly shifts its fluorescence emission

341 from green to red due to tyrosine oxidation and can be used as a molecular clock to track protein

342 turnover (**Fig. 5A**).[22] We, therefore, localized GEM-SCOPe-Timer to the mitochondria (COX8A-

343   Timer), to further investigate mitochondrial turnover[83,84] (**Fig. 5B**). To first validate COX8A-Timer,

344   mitophagy was inhibited by treating hiPSC-derived astrocytes transduced with COX8A-Timer with

345   the V-ATPase inhibitor bafilomycinA1 (BafA1). BafA1 treatment led to a significant increase in the

346   ratio of red-fluorescent mitochondria over green-fluorescent mitochondria compared to vehicle

347   control astrocytes (unpaired t-test, $p < 0.0001$; **Fig. 5C, D**). Since mitochondrial degradation and

348   turnover occur primarily through mitophagy, inhibition of mitophagy and mitochondrial recycling

349   via BafA1 treatment results in a predicted increase in longer-lived mitochondria.

350   Because PRKN is directly involved in mitophagy, and we observed impaired retrograde

351   mitochondrial transport in *PRKN*^{-/-} neurons, we wanted to measure changes in mitochondrial

352   turnover in human *PRKN*^{-/-} cells. We transduced wild-type (*PRKN*^{+/+}) and *PRKN* knockout *(PRKN*

353   [-/-]*)* hiPSC-derived astrocytes with GEM-SCOPe COX8A-Timer. The ratio of red-fluorescent signal

354   over green-fluorescent signal significantly increased in *PRKN*^{-/-} astrocytes compared to *PRKN*^{+/+}

355   astrocytes (unpaired t-test, $p = 0.026$, **Fig. 5E, F**). When broken down by individual channel, there

356   was no change in the green fluorescence (2-way ANOVA with Sidak correction, p-adj = 0.1288,

357   **Fig. 5G**), indicating no change in mitochondrial biogenesis. The increase in red to green ratio was

358   driven by a significant increase in red-fluorescent signal (2-way ANOVA with Sidak correction, p-

359   adj = 0.0005, **Fig. 5G**), which is in concordance with an accumulation of older mitochondria due

360   to a failure to properly degrade mitochondria in the absence of PRKN.

361   An expected consequence of impaired mitochondrial recycling is an accumulation of damaged

362   mitochondria and an increase in mitochondria-associated reactive oxygen species (ROS) from

363   inefficient cellular respiration. To measure reactive oxygen levels in live astrocytes, we introduced

364   GRX1-roGFP2, an established fluorophore for measuring ROS, into GEM-SCOPe[25]. GRX1-

365   roGFP2 is a fusion protein between GRX1 and roGFP2. When GRX1 is oxidized by glutathione,

366   it can subsequently oxidize roGFP2. Oxidized roGFP2 shifts its emission spectrum from green

367   fluorescence to blue fluorescence (**Fig. 6A**)[25,85]. Thus, the ratio of green to blue fluorescence is

368   an indicator of glutathione oxidation state. When GRX1-roGFP2 is further coupled with a

369   mitochondrial localization sequence, we can measure the oxidative stress of the mitochondria.

370   This construct was available as a retroviral vector using the signal sequence from *Neurospora*

371   *crassa* ATP synthase protein 9[25]. When we cloned it into the FUW lentivirus backbone, we decided

372   to keep that localization sequence rather than replace it with the signal sequence for COX8A used

373   in the other GEM-SCOPe mitochondria-localized fluorophores (**Fig. 6B**). To validate GEM-SCOPe

374   GRX1-roGFP2 was working as expected, hiPSC-derived astrocytes transduced with mito-GRX1-

375   roGFP2 were treated with BafA1 to induce oxidative stress[86]. Astrocytes treated with BafA1 had

376   a significant decrease in the ratio of green fluorescence to blue fluorescence when compared to

377   vehicle (DMSO) treated astrocytes (unpaired t-test, $p < 0.0001$, **Fig. 6C, D**). The effect is driven

378   by a significant increase specifically in blue fluorescence (2-way ANOVA with Sidak correction, p-

379   adj < 0.0001, **Fig. 6E**) while the green fluorescence remained unchanged (2-way ANOVA with

380   Sidak correction, p-adj = 0.99, **Fig. 6E**). The increase in blue fluorescence is due to an increase

381   in roGFP2 oxidation, which is indicative of an increase in glutathione oxidation and the presence

382   of reactive oxygen species. Thus, GEM-SCOPe-mito-GRX1-roGFP can be used to monitor

383   glutathione reduction potential and how cells respond to reactive oxygen stress.

384   Because astrocytes play important metabolically supportive roles in the CNS and we observed

385   PRKN-related impairments to mitochondrial recycling with COX8A-Timer (**Fig. 5E-G**), we wanted

386   to understand if PRKN deficiency has effects on ROS production in astrocytes. We transduced

387   *PRKN*^{+/+} and *PRKN*^{-/-} astrocytes with mito-GRX1-roGFP2 lentivirus. Without introducing any

388   additional chemical mitochondrial stressors, we observed an siginificant reduction in the ratio of

389   green-fluorescence signal to blue-fluorescence signal in *PRKN*^{-/-} compared to *PRKN*^{+/+} astrocytes

390   (unpaired t-test, p = 0.026; **Fig. 6F, G**). This is indicative of an increase in ROS in *PRKN*^{-/-}

391   astrocytes which correlates with our other observation of decreased mitochondrial turnover in the

392   same cells. It has been previously demonstrated that *PRKN*^{-/-} hiPSC-derived dopaminergic

393   neurons show increased cellular ROS[15] and *PRKN*^{-/-} mice have decreased antioxidant capabilities

394   and increased ROS-related protein and lipid damage[87]. By introducing fluorophore-biosensors

395   into our lentiviral catalog, we were able to expand the phenotypes we can observe in live cells to

396   measure changes in the intracellular environment in response to chemical and genetic

397   perturbations.

398

Discussion

399

400   Here, we developed and validated GEM-SCOPe (Genetically Engineered, Modular, SubCellular

401   Organelle Probes), a collection of subcellularly targeted fluorophores encoded in a lentiviral

402   backbone. By exploiting the modular design of the constructs, we easily cloned fluorophores with

403   different excitation/emission spectra specified to localize to the nucleus, lysosomes, or

404   mitochondria. We demonstrated that these fluorophores specifically localize to the desired

405   organelle and can quantitatively assess cellular responses to chemical perturbations. Finally, we

406   applied GEM-SCOPe to human *PRKN*-knockout astrocytes and neurons, which revealed

407   widespread perturbations to cellular proliferation, lysosomal distribution, and mitochondrial

408   dynamics, providing new insights into PD pathogenesis.

409   Gliosis has been widely reported in human post-mortem brain studies of patients with *PRKN* loss-

410   of-function mutations[88-91]. Similar pro-inflammatory phenotypes have also been observed in

411   mouse models and stem-cell-derived glial models of PRKN deficiency[92,93]. However, there is still

412   a limited understanding of how genetic mutations related to PD modify astrocytes and their role

413   in neurodegeneration. We used GEM-SCOPe to investigate cellular, mitochondrial, and lysosomal

414   dynamics in astrocytes lacking functional PRKN protein. Using nucleus-localized fluorophores,

415   we show that *PRKN* knockout human astrocytes have increased cellular proliferation compared

416   to isogenic, wild-type astrocytes. LAMP1-localized fluorophores revealed that lysosomes in *PRKN*

417   knockout astrocytes are distributed further from the perinuclear nuclear area. Finally, a variety of

418   mitochondria-localized fluorophores revealed that *PRKN* knockout astrocytes have impaired

419   mitochondrial transport, decreased mitochondrial turnover, increased reactive oxygen species,

420   and oxidized glutathione. While additional experiments should be done to support these findings,

421   GEM-SCOPe highlights that there is extensive dysregulation and disruption to normal organelle

422   dynamics in human *PRKN* astrocytes that warrants further investigation.

423   GEM-SCOPe was developed in a 3rd generation lentiviral system. We selected this delivery

424   system because 1) lentiviruses are safe to produce; 2) they infect both dividing and non-dividing

425   cells; and 3) they can be used to develop stable cell lines. 3rd generation lentiviral systems are

426   replication-incompetent, so cells that are transduced with lentivirus cannot produce more viral

427   particles. Only the transfer plasmid, which contains the insert of interest, can be integrated into

428   the host genome; the other plasmids that encode lentiviral structural and envelope genes do not

429   integrate into the host genome, preventing viral replication. Most lentiviruses are produced with

430   VSV-G (Vesicular stomatitis virus G glycoprotein) as the envelope protein, as it provides broad

431   tropism and enables high transduction efficiency in a wide variety of cell types[94]. Finally, GEM-

432   SCOPe lentiviruses were developed with the option to include an antibiotic-resistance gene (**Fig.**

433   **1A**), which can be used to establish stable cell lines that have incorporated the lentiviral load.

434   Although lentiviruses provide a lot of flexibility and safety when delivering genetic information,

435   they also possess some limitations. Lentiviruses have an ideal plasmid size of 9-10kb, and viral

436   titer can decrease if plasmids exceed this size[95]. The H2B-mTagBFP2, H2B-mCherry, and H2B-

437   Emerald lentiviruses (**Fig. 1, 2**) are about 11kb each and transduced hiPSC-derived astrocytes

438   with about 90% efficiency. Coupled with the puromycin resistance that was also included in this

439   construct, we were still able to generate a population with 100% viral transduction despite the size

440   limitation. Another drawback of lentiviral gene delivery is that inserts often integrate into actively

441   transcribed loci[96]. Differentiation of hiPSCs into specific cell types requires extensive chromatin

442   remodeling, and genomic sequences integrated via lentivirus can often be silenced in this

443   process. In the case where hiPSCs must be transduced before differentiation, antibiotic selection

444   during differentiation can select for cells that have integrated the viral load into a genomic region

445   that is not silenced. The final drawback of lentiviral gene delivery is that fluorescence intensity is

446   dependent on the viral copy number in each cell and cannot be used as a readout for organelle

447   abundance. Rather, we need to use measurements like distribution, size, and ratios of different

448   emissions within the same cell. This is not just a limitation of lentiviral gene delivery but of other

449   viral and non-viral delivery systems.

450   In this study, we focused on PD and specifically the alterations to astrocytes with *PRKN* mutations.

451   However, alterations in proliferation, mitochondria, and lysosomes are by no means unique to PD.

452   Many reviews cover the extensive roles of mitochondria and lysosomes in health and disease[97-

453   100]. GEM-SCOPe can be applied beyond neuronal cells and neurodegeneration to countless other

454   cell types to investigate subcellular dynamics that affect disease development and progression.

455   Due to its modular design, GEM-SCOPe can be expanded and molded by research groups to

456   meet specific needs. Different targeting sequences can be integrated to localize fluorophores to

457   relevant subcellular compartments. New fluorophores and biosensors are always being

458   developed to measure additional intracellular conditions. By applying GEM-SCOPe to disease

459   models, we will be able to better understand how cells are disrupted over the course of disease

460   progression, providing insight for future therapeutic targets.

461

Acknowledgements

Author Contributions

Conceptualization, C.G., T.A., and J.W.B.; Methodology, C.G., L.S., and T.A.; Validation, C.G.; Formal Analysis, C.G.; Investigation, C.G., T.K., L.S., and A.S.; Resources, C.G., T.K., L.S., and B.R.S.; Writing – Original Draft, C.G. and J.W.B.; Writing – Review & Editing, C.G., L.S., B.R.S., and J.W.B.; Visualization, C.G.; Funding Acquisition, T.A. and J.W.B.

Declaration of Interests

The authors declare no competing interests

Materials and Methods

Experimental model and study participant details

The human cell lines used in this study are detailed in the key resources table and below.

HEK293FT (RRID: CVCL_6911, fetal kidney origin, female sex) were maintained in DMEM (Gibco 10566) supplemented with 10% bovine calf serum (Cytiva SH30073) at 37 °C in a 5% CO_2 incubator. Cells were passaged ever 4-5 days, when they reached 90% confluency.

H1(WA01) hESCs (male), BJ-SiPS-D iPSCs (male), and AG09173 iPSCs (female) were maintained in StemFlex medium (Gibco A3349401) at 37 °C in a 5% CO_2 incubator. Cells were passaged every 3-4 days, when they reached 90% confluency. WA01 astrocytes were used for all PRKN-genotype dependent experiments. BJ-SiPS-D and AG09173 were used for organelle localization validation and chemical perturbation validation.

Molecular cloning

All vectors were derived from pFUW (Addgene plasmid #14882). pFUW was linearized using NheI-HF (NEB R3131) and BamHI-HF (NEB R3136) per manufacturer's protocol, and the desired fragment was gel-purified (Macherey-Nagel 740609). Components of the insert were PCR amplified using Q5-Hot Start DNA Polymerase (NEB M0493) per manufacturer's recommendations. Fluorophores were amplified from commercially available plasmids (see

503   Resource Table for complete list) and localization sequences were amplified from cDNA. Primers

504   were designed using the NEBuilder Assembly Tool (nebuilder.neb.com) to add 5' and 3'

505   sequences that make the fragments compatible for Gibson assembly and ordered from IDT

506   (Integrated DNA Technologies). Gibson reactions were set up with NEBuilder HiFi DNA Assembly

507   Master Mix (NEB E2621), 50ng of linearized backbone, and 3-fold molar excess of each PCR

508   fragment. For fragments less than 200bp, 5-fold molar excess was used. Reactions were

509   incubated at 50°C for 60 minutes. The Gibson product was transformed in 10-beta competent *E.*

510   *coli* (NEB C3019) grown on LB Agar plates with 100ug/mL ampicillin. Plasmids from single clones

511   were isolated via miniprep (Macherey-Nagel 740499) and sequenced to confirm successful

512   cloning.

513

514   Lentivirus Production

515   Lentivirus was produced by transfection of HEK293T cells as adapted from Dull et al. 1998 [101].

516   HEK293T cells were grown in Dulbecco's Modified Eagle Medium (DMEM; Gibco 11965092) with

517   10% bovine calf serum (Cytiva SH30073) at 37 °C in a 5% CO_2 incubator. The day before

518   transfection, ~10^7 cells were plated per 15cm dish coated in 0.1% gelatin. Media was changed

519   just prior to transfection. For one 15cm dish, 22.5ug of transfer vector was combined with 14.7ug

520   of pMDLg/pRRE (Addgene plasmid #12251), 5.7ug of pRSV.Rev (Addgene plasmid #12253), and

521   7.9ug of pMD2.G (Addgene plasmid #12259) in a 15mL conical tube. The plasmid mixture was

522   added to 1mL of 278 uM $CaCl_2$ (Sigma C1016) and mixed thoroughly before adding 1mL of 2x

523   BBS solution [280 mM NaCl (Fisher Scientific S271-1), 50 mM BES (Millipore 391334), 1.5mM

524   Na_2HPO_4 (Sigma S5136); pH = 6.95] dropwise. Tubes were mixed by inversion, incubated at room

525   temperature for 1 min, and then added dropwise to HEK293T dish. Cell culture media was

526   changed after 16-24 h. Conditioned media was then collected every 24 h for 2 days; conditioned

527   media from the same plate was combined over the two collections. Conditioned media was

528   centrifuged at 2000 x g for 10 minutes to pellet debris and filtered through 0.22-um-pore-size PES

529   filter (Millipore SCGP00525). To concentrate virus, filtered media was incubated with PEG 8000

530   (Sigma P2139) and NaCl, at a final concentration of 5% and 0.15M respectively, overnight at 4°C,

531   then centrifuged at 3000 x g for 20 min. The pellet was resuspended in DMEM/F12 with GlutaMAX

532   (Gibco 10565018) to 1% of the original supernatant volume. The concentrated virus was stored

533   in aliquots at -80°C.

534

Midbrain Organoid and Astrocyte Differentiation

536   hiPSC-derived astrocytes were extracted from 100-day-old midbrain organoids as described in

537   Sarrafha et al 2021 and Parfitt et al 2024 [81,102]. In short, hiPSCs were cultured in StemFlex medium

538   (Gibco A3349401) at 37 °C in a 5% CO_2 incubator. hiPSCs were seeded into 125-mL spinner

539   flasks (Corning 3152) and allowed to self-aggregate in StemFlex (Gibco A3349401)

540   supplemented with 10 μM Y-27632 (Tocris 1254) and 1% Penicillin-Streptomycin (Gibco

541   15140122). Once aggregates were between 300 μm and 500 μm, differentiation was initiated by

542   dual-SMAD inhibition with 10 μM SB431542 (Stemgent 04-0010), 100nM LDN193189 (Tocris

543   6053), 1x B27 without Vitamin A (Gibco 12587010) and 1x N2 (Gibco 17502048) in DMEM-F12

544   with GlutaMAX (Gibco 10565018). Midbrain patterning was achieved with the addition of 3 μM

545   CHIR99021 (Tocris 4423), 2 μM purmorphamine (Stemcell 72204), and 1 μM SAG (Cayman

546   11914) starting 4 days after neural induction. After patterning, media was changed to DMEM/F12

547   with GlutaMAX, supplemented with 1x N2, 1x B27 without Vitamin A, 20 ng/mL GDNF (Peprotech

548   450-10), 20 ng/mL BDNF (Peprotech 450-02), 200 μM L-ascorbic acid (Fisher Scientific BP351),

549   100 μM dibutyryl cAMP (Biogems 1698950), and 10 μM DAPT (Cayman 13197). After 35 days,

550   organoids were transferred to ultra-low attachment plates (Corning 3516), with about 5 organoids

551   per mL of media and cultured in DMEM/F12 with GlutaMAX supplemented with 1x N2, 1x B27

552   without Vitamin A, 10 ng/mL GDNF, 10 ng/mL BDNF, and 200 µM ascorbic acid.

553   Astrocytes were extracted from midbrain organoids starting at day 100. Organoids were gently

554   dissociated in a trypsin enzyme solution (TrypLE Select, Gibco 12563011) using a glass pipette

555   to break up organoids into large chunks. The organoid chunks from 5-10 organoids were placed

556   on 15cm dishes coated with 0.1% gelatin and maintained in Astrocyte Medium (AM; ScienCell

557   #1801). Astrocytes were allowed to grow out of the organoid chunks until the plate was confluent

558   (about 1 week). At this point, astrocytes can be cryopreserved. Astrocytes were maintained in AM

559   and switched to experimental media [1:1 DMEM/F-12:Neurobasal (Gibco 21103049), 1x B27

560   without Vitamin A, 1x N2, 1x MEM-Non-Essential Amino Acids (Gibco 11140050), 1x GlutaMAX

561   (Gibco 35050061), 10 ng/mL CNTF (Peprotech 450-13)] 2-3 days before imaging.

562

Astrocyte Viral Transduction

563

564   iPSC-derived astrocytes were transduced during regular passaging. In short, astrocytes were

565   lifted, spun down, resuspended in AM media, and divided into 1.5mL microcentrifuge tubes,

566   depending on the desired split ratio and number of transductions. The virus was added to the cell

567   suspension and incubated for 5-10 minutes before plating the mixture. Media was topped off such

568   that the final dilution of the virus in media was 1:50. Depending on the viral titer, this dilution

569   sometimes increased or decreased. Astrocytes can also be transduced without passage by

570   adding the virus directly to the media. Media is changed after 24 hours. Antibiotics were added to

571   the media, if relevant, starting at least 3 days after transduction.

572

MitoTracker and LysoTracker

573

574 For MitoTracker staining, astrocytes were incubated with 100 nM of MitoTracker DeepRed

575 (Thermo Scientific M22425) for 30 min at 37 °C. For LysoTracker staining, astrocytes were

576 incubated 100 nM of LysoTracker DeepRed (Thermo Scientific L12492) for 5 min at 37 °C. Cells

577 were then washed twice with PBS before incubation with Hoechst 33342 (Thermo Scientific

578 62249).

579

qPCR

580

581 RNA was extracted from samples using TRIzol (Invitrogen 15596018) and an RNA extraction kit

582 following the manufacturer's recommended protocol (Zymo R2062). RNA concentration and purity

583 were measured on a spectrophotometer. cDNA was produced from 1 ug of RNA per sample, using

584 Maxima H Minus Reverse Transcriptase (Thermo Scientific EP0752) and following the

585 manufacturer's recommendations. qPCR reactions were prepared in a 384-well plate (Applied

586 Biosystems 4309849) with 1:10 dilution of cDNA, 2x PowerUp SYBR Green Master Mix (Applied

587 Biosystems A25741) and 1 µM each of forward and reverse primers. qPCRs were run on

588 QuantStudio 7 (Applied Biosystems 4485701) and analyzed using the ΔΔCt method, normalized

589 to *ACTB*. The following primers were used:

590 *ACTB* Forward: CCTGGCACCCAGCACAAT

591 *ACTB* Reverse: GCCGATCCACACGGAGTA

592 *LAMP1* Forward: CAGATGTGTTAGTGGCACCCA

593 *LAMP1* Reverse: TTGGAAAGGTACGCCTGGATG

594

Live Cell Imaging

In general, astrocytes were seeded at 10 x 10³ cells per well of a 96-well plate with a cover glass thickness polystyrene bottom (Greiner 655090) coated in 0.1% gelatin 3-5 days before imaging. Proliferation assays were seeded at 8 x 10³ cells per well and started 1 day after seeding. Before imaging, cells were incubated with Hoechst 33342 (Thermo Scientific 62249) or DRAQ5 (Thermo Scientific 52251) for 10 minutes.

Wide-field live cell imaging was performed using the Thermo Scientific CX7 High Content Screening Platform with 20x and 40x objective lenses (LUCPLFLN20x and LUCPLFLN40x). The microscope was equipped with an incubation unit that maintained temperature, CO_2, and humidity during image acquisition. Confocal images were acquired on a Nikon Ti2E AX R confocal microscope with a 20x objective lens (PLAN APO λD 20x) and 6x optical zoom. Each well was imaged in 5 (confocal) or 25-36 (widefield) different areas, with the average of those images represented as a single data point.

ImageJ Image Analysis

Nuclear Proliferation: Nuclear proliferation was quantified by converting images to a binary based on a threshold and then using 'Analyze Particles' to obtain a count for the number of nuclei in a field. The same threshold and parameters were kept for all time points.

Mitochondrial Fragmentation: Mitochondrial fragmentation was measured using the ImageJ plugin, Mitochondrial Analyzer [103]. For thresholding, the "Block Size" was set to 1.45 microns and the "C-Value" was set to 5.

616 <u>Ratiometric Quantification:</u> Ratiometric quantifications for roGFP2, Timer, and Lemon were

617 achieved by measuring the mean grey value in both channels of interest. The values for each

618 channel were then divided to generate the ratio of relative intensity between the two channels.

619 <u>Kymograph Analysis:</u> Kymograph analysis of mitochondrial movement was achieved using the

620 Image J plugins KymographClear 2.0 and KymographDirect [104]. KymographClear 2.0 was used

621 to trace mitochondrial trajectories and generate kymographs from which stationary and motile

622 mitochondria were identified. KymographDirect was then used to extract quantitative information

623 from the trajectories of the motile mitochondria.

624

Cell Profiler Image Analysis [72,105]

626 <u>Subcellular Co-localization:</u> For nuclear co-localization, nuclei in the genetically encoded

627 fluorophore channel and the DRAQ5 channel were identified, and nuclei from cells that were not

628 transduced were filtered out. For lysosomal and mitochondrial co-localization, propagation from

629 the nuclear stain was used to identify cell bodies. Cells were filtered to only analyze those with

630 lentivirus signal within the cell body. Co-localization was reported as the Mander's coefficient

631 indicating the overlap of the genetically encoded fluorophore with the commercially available

632 stain.

633 <u>Lysosomal Distribution:</u> Cells were defined by nuclei and full cell fluorophore signal. Lamp1-

634 mCherry signal was assigned to the cell body with which it overlapped. Only cells that were

635 successfully transduced were included in the analysis. The distribution of the Lamp1-mCherry

636 signal was calculated using the "MeasureObjectIntensityDistribution" with two bins generated for

637 each cell using the nuclei as the center of the cell. Bins were scaled such that the inner bin

638 (perinuclear) was always the same percent of total cell area regardless of cell size.

639

Quantification and statistical analysis

All experiments were conducted with 3-6 replicates. All quantifications were represented as mean ± standard deviation, except for the violin plots of the kymograph analysis. Details on data visualization, sample size, and images per replicate are included in figure captions. Details on statistical tests and significance are included in the text. All statistical tests were conducted in *GraphPad Prism* and graphs were generated in *GraphPad Prism*.

646

Figure Legends

Fig. 1: A toolbox of lentiviral plasmids developed and validated for subcellular localization of fluorophores (A) Schematic of lentiviral plasmids highlighting the combinatorial power of the toolbox components. Generated using BioRender **(B)** Schematic demonstrating the cloning strategies used to generate the constructs used in this study as well as any future constructs. Generated using BioRender **(C)** Representative images of subcellular localization validation with available dyes in hiPSC-derived astrocytes and Mander's co-efficient for overlap of the genetically encoded fluorophore with the dye. Bars represent mean values and error bars represent standard deviation. Top: H2B-mTagBFP2 and DRAQ5 (n = 3; each replicate is an average over 16 images); Middle: LAMP1-mCherry and LysoTracker Deep Red; nuclei stained with Hoechst33342 (n = 4; each replicate is an average over 4 images); Bottom: COX8A-Emerald and MitoTracker Deep Red; nuclei stained with Hoechst33342 (n = 3, each replicate is an average over 36 images). Scale bars = 50 μm **(D)** Representative images of combinatorial applications of GEM-SCOPe.

660   Top: Cell expressing LAMP1-Emerald and COX8A-mCherry. Bottom: cell expression LAMP1-

661   mCherry and COX8A-Emerald. Nuclei were stained with DRAQ5. Scale bars = 50 μm.

662   **Fig. 2: Nucleus-localized fluorophores offer improvements over available stains for**

663   **multiday imaging (A)** Schematic of the lentiviral construct localizing mTagBFP2 to the nucleus

664   with an H2B fusion protein and antibiotic resistance to puromycin used in the following panels **(B)**

665   Representative images of H2B-mTagBFP2 and DRAQ5 nuclear stain 1 hour (top) and 24 hours

666   (bottom) after adding DRAQ5 to the cell cultures. **(C)** Quantification of the percent of stain

667   localized to the nuclear area versus the cytoplasm 1 hour and 24 hours after adding DRAQ5 to

668   cell cultures. The central bar represents the mean and the error bars represent the standard

669   deviation (n = 3 per time point; each replicate is an average over 36 images) **(D)** Schematic of the

670   lentiviral construct localizing Emerald or mCherry to the nucleus with an H2B fusion protein and

671   antibiotic resistance to puromycin used in the following panels **(E)** Representative images of

672   nuclei from $PRKN^{+/+}$ astrocytes, labeled with H2B-Emerald, and $PRKN^{-/-}$ astrocytes, labeled with

673   H2B-mCherry, cultured together during a proliferation assay. Images were taken 24 hours (top)

674   after seeding and 72 hours (bottom) after seeding **(F)** Quantification of number of $PRKN^{+/+}$ and

675     $PRKN^{-/-}$ nuclei per image field 24 hours and 72 hours after seeding. Dots represent mean values

676   and error bars represent standard deviation (n = 3 per time point; each replicate is an average

677   over 25 images). Scale bars = 50 μm. All images were acquired on the CX7 HCS platform with a

678   20x objective lens.

679   **Fig. 3: Lysosome-localized fluorophores reveal changes in lysosomal distribution upon**

680   **chemical and genetic perturbation (A)** Schematic of the lentiviral constructs used in the

681   following panels localizing (top) mCherry to the lysosome with the 5' sequence of *LAMP1* and

682   (bottom) Emerald to the whole cell by not including a localization sequence. **(B)** Representative

683   images of astrocytes transduced with Emerald and LAMP1-mCherry lentiviruses and treated with

684   100 nM bafilomycin A1 (bottom) or a vehicle (DMSO; top). Nuclei were stained with

685   Hoechst33342. Far right: Output from CellProfiler showing the distribution Lamp1-mCherry signal

686   as a fraction of signal in each bin. Darker blue indicates a higher fraction of signal in that bin.

687   Scale bars = 50 µm. **(C)** Quantification of lysosomal number per cell (left), average vesicle area

688   (middle) and fraction of perinuclear lysosomes (right) using Lamp1-mCherry signal in vehicle

689   (DMSO) and bafilomycin A1 (100 nM) treated astrocytes. Emerald was used to determine cell

690   boundaries. Central bars represent mean and error bars represent standard deviation (n = 4; each

691   replicate is an average over 10 images). **(D)** Representative images of *PRKN*$^{+/+}$ (top) and *PRKN*$^{-}$

692     $^{/-}$ (bottom) astrocytes transduced with cytoplasmic Emerald and LAMP1-mCherry lentiviruses.

693   Nuclei were stained with Hoechst33342. Far right: Output from CellProfiler showing the

694   distribution Lamp1-mCherry signal as a fraction of signal in each bin. Darker blue indicates a

695   higher fraction of signal in that bin. Scale bars = 25 µm. (**E**) Quantification of Lamp1-mCherry

696   signal in *PRKN*$^{+/+}$ and *PRKN*$^{-/-}$ astrocytes to measure lysosomal number per cell (left), average

697   vesicle area (middle) and fraction of perinuclear lysosomes (right). Emerald fluorescence was

698   used to determine cell boundaries. Central bars represent mean and error bars represent

699   standard deviation (n = 6; each replicate is an average over 7 images). All images were acquired

700   on a Nikon Ti2E AX R confocal microscope with a 20x objective lens and 6x optical zoom.

701   **Fig. 4: Mitochondria-localized fluorophores resolve changes in mitochondrial network**

702   **dynamics (A)** Schematic of the lentiviral construct used in the following panels localizing Emerald

703   to the mitochondria with the targeting sequence of COX8A. **(B)** Representative images of

704   astrocytes transduced with COX8A-Emerald and treated with a vehicle (DMSO; top) or 2 uM

705   oligomycin (bottom). Nuclei were stained with Hoechst33342. High magnification images (far

706   right) highlight the changes to the mitochondrial network upon oligomycin treatment. Scale bars

707   = 50 µm. **(C)** Quantification of mean mitochondrial area, mean mitochondrial branch length, and

708   mean aspect ratio upon oligomycin treatment. Central bars represent mean and error bars

709   represent standard deviation (n = 3; each replicate is an average over 36 images) **(D)**

710   Representative images of mitochondria labeled with COX8A-Emerald moving along *PRKN$^{-/-}$*

711   neuron axons in the anterograde (left) and retrograde (right) directions. Scale bars = 5 μm. Images

712   were taken on a Leica DMi8 microscope for 1 hour per field **(E-F)**. Quantification of mitochondrial

713   run length (left) and run time (right) of COX8A-Emerald labeled mitochondria in *PRKN$^{+/+}$* and

714   *PRKN$^{-/-}$* dopaminergic neuron axons moving anterograde (E) and retrograde (F) as determined

715   by kymograph analysis (average of n = 37.5 organoids for anterograde and 23.5 organoids for

716   retrograde; each replicate is an average over 1-3 fields).

717   **Fig. 5: Timer fluorophore measures changes in subcellular mitochondrial turnover in**

718   ***PRKN$^{-/-}$*(A)** Schematic demonstrating how the fluorescent protein Timer works. Timer undergoes

719   a fluorescent shift from a green emission to a red emission overtime; analysis of Timer relies on

720   examining the ratio between the red and green emission. **(B)** Schematic of the lentiviral construct

721   used in the following panels localizing Timer to the mitochondria by using the targeting sequence

722   of COX8A. **(C)** Representative images of astrocytes transduced with COX8A-Timer and treated

723   with a vehicle (DMSO; top) or 100 nM bafilomycin A1 (bottom) for 24 hours. Images were acquired

724   with a 488-excitation line and a 594-excitation line. Far right: ratiometric representation of the red

725   channel divided by the green channel and pseudo colored so that orange, yellow and white

726   indicate more relative red emission and black and purple indicate more relative green emission.

727   Nuclei were stained with DRAQ5. Scale bars = 50 μm. **(D)** Quantification of the ratio of mean

728   intensity of emission from excitation with a 594nm laser to the mean intensity of emission from

729   excitation with a 488 nm laser in astrocytes expressing COX8A-Timer and treated with a vehicle

730   (DMSO) or 100 nM bafilomycin A1 for 24 hours. Central bars represent mean and error bars

731   represent standard deviation (n = 6; each replicate is an average over 25 images). (**E**)

732   Representative images of *PRKN$^{+/+}$* and *PRKN$^{-/-}$* astrocytes transduced with COX8A-Timer.

733   Images were acquired with a 488-excitation line and a 594-excitation line. Far right: ratiometric

734   representation of the red channel divided by the green channel and pseudo colored so that

735   orange, yellow and white indicate more relative red emission and black and purple indicate more

736   relative green emission. Nuclei were stained with DRAQ5. Scale bars = 50 μm. **(F)** Quantification

737   of the ratio of mean intensity of emission from excitation with a 594nm laser to the mean intensity

738   of emission from excitation with a 488 nm laser in *PRKN*$^{+/+}$ and *PRKN*$^{-/-}$ astrocytes expressing

739   COX8A-Timer. Central bars represent mean and error bars represent standard deviation (n = 3;

740   each replicate is an average over 25 images). **(G)** Quantification of mean intensity normalized by

741   nuclear area of green and red fluorescence in *PRKN*$^{+/+}$ and *PRKN*$^{-/-}$ astrocytes expressing

742   COX8A-Timer. Central bars represent mean and error bars represent standard deviation (n = 3;

743   each replicate is an average over 25 images). All images were acquired on a CX7 HCS platform

744   with a 20x objective lens.

745   **Fig. 6: GRX1-roGFP2 fluorophore is used to quantify glutathione oxidation in chemical and**

746   **genetic models of oxidative stress (A)** Schematic demonstrating how the fluorescent protein

747   fusion Grx1-roGFP2 works. Oxidation of Grx1 upon the oxidation of glutathione results in the

748   eventual oxidation of roGFP2, shifting its emission spectrum from green to blue. **(B)** Schematic

749   of the lentiviral construct used in the following panels localizing Grx1-roGFP2 to the mitochondria.

750   This fluorophore was localized using atp-9 instead of COX8A. **(C)** Representative images of

751   astrocytes transduced with mito-GRX1-roGFP2 and treated with a vehicle (DMSO; top) or 100

752   nM bafilomycin A1 (bottom) for 24 hours. Images were acquired with a 405-excitation laser and a

753   488-excitation laser. Far right: ratiometric representation of the green channel divided by the blue

754   channel and then pseudo colored so that orange, yellow and white indicate more relative green

755   emission while black and purple represent more blue emission. Nuclei were stained with DRAQ5.

756   Scale bars = 50 μm. **(D)** Quantification of the ratio of mean intensity from 488-excitation to the

757   mean intensity from 405 excitation. In astrocytes expression mito-Grx1-roGFP2 and treated with

758   a vehicle or 100 nM bafilomycin A1. Central bars represent mean and error bars represent

759   standard deviation (n = 6; each replicate is an average over 25 images). **(E)** Quantification of

760 mean intensity normalized by nuclear area of blue and green fluorescence in vehicle and

761 bafilomycin A1 treated astrocytes expressing mito-Grx1-roGFP2. Central bars represent mean

762 and error bars represent standard deviation (n = 6; each replicate is an average of 25 images).

763 **(F)** Representative images of *PRKN^{+/+}* and *PRKN^{-/-}* astrocytes transduced with mito-Grx1-

764 roGFP2. Images were acquired with a 405-excitation laser and a 588-excitation laser. Far right:

765 ratiometric representation of the green channel divided by the blue channel and pseudo colored

766 so that orange, yellow and white indicate more relative green emission and black and purple

767 indicate more relative blue emission. Nuclei were stained with DRAQ5. Scale bars = 50 µm. **(G)**

768 Quantification of the ratio of mean intensity of emission from excitation with a 488nm laser to the

769 mean intensity of emission from excitation with a 405 nm laser in *PRKN^{+/+}* and *PRKN^{-/-}* astrocytes

770 expressing mito-Grx1-roGFP2. Central bars represent mean and error bars represent standard

771 deviation (n = 3; each replicate is an average over 16 images).

772

773

References

775 1. Willis, A.W., Roberts, E., Beck, J.C., Fiske, B., Ross, W., Savica, R., Van Den Eeden,

776 S.K., Tanner, C.M., Marras, C., and Parkinson's Foundation, P.G. (2022). Incidence of

777 Parkinson disease in North America. NPJ Parkinsons Dis *8*, 170. 10.1038/s41531-022-

778 00410-y.

779 2. Vazquez-Velez, G.E., and Zoghbi, H.Y. (2021). Parkinson's Disease Genetics and

780 Pathophysiology. Annu Rev Neurosci *44*, 87-108. 10.1146/annurev-neuro-100720-

781 034518.

782   3.   Schneider, S.A., and Obeso, J.A. (2015). Clinical and pathological features of

783   Parkinson's disease. Curr Top Behav Neurosci *22*, 205-220. 10.1007/7854_2014_317.

784   4.   Varadi, C. (2020). Clinical Features of Parkinson's Disease: The Evolution of Critical

785   Symptoms. Biology (Basel) *9*. 10.3390/biology9050103.

786   5.   Jankovic, J. (2008). Parkinson's disease: clinical features and diagnosis. J Neurol

787   Neurosurg Psychiatry *79*, 368-376. 10.1136/jnnp.2007.131045.

788   6.   Naoi, M., and Maruyama, W. (1999). Cell death of dopamine neurons in aging and

789   Parkinson's disease. Mech Ageing Dev *111*, 175-188. 10.1016/s0047-6374(99)00064-0.

790   7.   Spillantini, M.G., Schmidt, M.L., Lee, V.M., Trojanowski, J.Q., Jakes, R., and Goedert, M.

791   (1997). Alpha-synuclein in Lewy bodies. Nature *388*, 839-840. 10.1038/42166.

792   8.   Ohama, E., and Ikuta, F. (1976). Parkinson's disease: distribution of Lewy bodies and

793   monoamine neuron system. Acta Neuropathol *34*, 311-319. 10.1007/BF00696560.

794   9.   Hartmann, A. (2004). Postmortem studies in Parkinson's disease. Dialogues Clin

795   Neurosci *6*, 281-293. 10.31887/DCNS.2004.6.3/ahartmann.

796   10.   Helmchen, F., Fee, M.S., Tank, D.W., and Denk, W. (2001). A miniature head-mounted

797   two-photon microscope. high-resolution brain imaging in freely moving animals. Neuron

798   *31*, 903-912. 10.1016/s0896-6273(01)00421-4.

799   11.   Zong, W., Wu, R., Li, M., Hu, Y., Li, Y., Li, J., Rong, H., Wu, H., Xu, Y., Lu, Y., et al.

800   (2017). Fast high-resolution miniature two-photon microscopy for brain imaging in freely

801   behaving mice. Nat Methods *14*, 713-719. 10.1038/nmeth.4305.

802   12.   Chen, K., Tian, Z., and Kong, L. (2022). Advances of optical miniscopes for in vivo

803   imaging of neural activity in freely moving animals. Front Neurosci *16*, 994079.

804   10.3389/fnins.2022.994079.

805   13.   Potashkin, J.A., Blume, S.R., and Runkle, N.K. (2010). Limitations of animal models of

806   Parkinson's disease. Parkinsons Dis *2011*, 658083. 10.4061/2011/658083.

807 14. Chia, S.J., Tan, E.K., and Chao, Y.X. (2020). Historical Perspective: Models of

808 Parkinson's Disease. Int J Mol Sci *21*. 10.3390/ijms21072464.

809 15. Ahfeldt, T., Ordureau, A., Bell, C., Sarrafha, L., Sun, C., Piccinotti, S., Grass, T., Parfitt,

810 G.M., Paulo, J.A., Yanagawa, F., et al. (2020). Pathogenic Pathways in Early-Onset

811 Autosomal Recessive Parkinson's Disease Discovered Using Isogenic Human

812 Dopaminergic Neurons. Stem Cell Reports *14*, 75-90. 10.1016/j.stemcr.2019.12.005.

813 16. Raja, W.K., Neves, E., Burke, C., Jiang, X., Xu, P., Rhodes, K.J., Khurana, V.,

814 Scannevin, R.H., and Chung, C.Y. (2022). Patient-derived three-dimensional cortical

815 neurospheres to model Parkinson's disease. PLoS One *17*, e0277532.

816 10.1371/journal.pone.0277532.

817 17. Chlebanowska, P., Tejchman, A., Sulkowski, M., Skrzypek, K., and Majka, M. (2020).

818 Use of 3D Organoids as a Model to Study Idiopathic Form of Parkinson's Disease. Int J

819 Mol Sci *21*. 10.3390/ijms21030694.

820 18. Kim, H., Park, H.J., Choi, H., Chang, Y., Park, H., Shin, J., Kim, J., Lengner, C.J., Lee,

821 Y.K., and Kim, J. (2019). Modeling G2019S-LRRK2 Sporadic Parkinson's Disease in 3D

822 Midbrain Organoids. Stem Cell Reports *12*, 518-531. 10.1016/j.stemcr.2019.01.020.

823 19. Shimomura, O., Johnson, F.H., and Saiga, Y. (1962). Extraction, purification and

824 properties of aequorin, a bioluminescent protein from the luminous hydromedusan,

825 Aequorea. J Cell Comp Physiol *59*, 223-239. 10.1002/jcp.1030590302.

826 20. Wang, M., Da, Y., and Tian, Y. (2023). Fluorescent proteins and genetically encoded

827 biosensors. Chem Soc Rev *52*, 1189-1214. 10.1039/d2cs00419d.

828 21. Ovechkina, V.S., Zakian, S.M., Medvedev, S.P., and Valetdinova, K.R. (2021).

829 Genetically Encoded Fluorescent Biosensors for Biomedical Applications. Biomedicines

830 *9*. 10.3390/biomedicines9111528.

831   22.   Terskikh, A., Fradkov, A., Ermakova, G., Zaraisky, A., Tan, P., Kajava, A.V., Zhao, X.,

832   Lukyanov, S., Matz, M., Kim, S., et al. (2000). "Fluorescent timer": protein that changes

833   color with time. Science *290*, 1585-1588. 10.1126/science.290.5496.1585.

834   23.   Nakai, J., Ohkura, M., and Imoto, K. (2001). A high signal-to-noise Ca(2+) probe

835   composed of a single green fluorescent protein. Nat Biotechnol *19*, 137-141.

836   10.1038/84397.

837   24.   Burgstaller, S., Bischof, H., Gensch, T., Stryeck, S., Gottschalk, B., Ramadani-Muja, J.,

838   Eroglu, E., Rost, R., Balfanz, S., Baumann, A., et al. (2019). pH-Lemon, a Fluorescent

839   Protein-Based pH Reporter for Acidic Compartments. ACS Sens *4*, 883-891.

840   10.1021/acssensors.8b01599.

841   25.   Gutscher, M., Pauleau, A.L., Marty, L., Brach, T., Wabnitz, G.H., Samstag, Y., Meyer,

842   A.J., and Dick, T.P. (2008). Real-time imaging of the intracellular glutathione redox

843   potential. Nat Methods *5*, 553-559. 10.1038/nmeth.1212.

844   26.   Nalls, M.A., Blauwendraat, C., Vallerga, C.L., Heilbron, K., Bandres-Ciga, S., Chang, D.,

845   Tan, M., Kia, D.A., Noyce, A.J., Xue, A., et al. (2019). Identification of novel risk loci,

846   causal insights, and heritable risk for Parkinson's disease: a meta-analysis of genome-

847   wide association studies. Lancet Neurol *18*, 1091-1102. 10.1016/S1474-4422(19)30320-

848   5.

849   27.   Karimi-Moghadam, A., Charsouei, S., Bell, B., and Jabalameli, M.R. (2018). Parkinson

850   Disease from Mendelian Forms to Genetic Susceptibility: New Molecular Insights into

851   the Neurodegeneration Process. Cell Mol Neurobiol *38*, 1153-1178. 10.1007/s10571-

852   018-0587-4.

853   28.   Jia, F., Fellner, A., and Kumar, K.R. (2022). Monogenic Parkinson's Disease: Genotype,

854   Phenotype, Pathophysiology, and Genetic Testing. Genes (Basel) *13*.

855   10.3390/genes13030471.

29.   Guadagnolo, D., Piane, M., Torrisi, M.R., Pizzuti, A., and Petrucci, S. (2021). Genotype-Phenotype Correlations in Monogenic Parkinson Disease: A Review on Clinical and Molecular Findings. Front Neurol *12*, 648588. 10.3389/fneur.2021.648588.

30.   Lesage, S., Lunati, A., Houot, M., Romdhan, S.B., Clot, F., Tesson, C., Mangone, G., Toullec, B.L., Courtin, T., Larcher, K., et al. (2020). Characterization of Recessive Parkinson Disease in a Large Multicenter Study. Ann Neurol *88*, 843-850. 10.1002/ana.25787.

31.   Pickrell, A.M., and Youle, R.J. (2015). The roles of PINK1, parkin, and mitochondrial fidelity in Parkinson's disease. Neuron *85*, 257-273. 10.1016/j.neuron.2014.12.007.

32.   Tanaka, K. (2020). The PINK1-Parkin axis: An Overview. Neurosci Res *159*, 9-15. 10.1016/j.neures.2020.01.006.

33.   Kamienieva, I., Duszynski, J., and Szczepanowska, J. (2021). Multitasking guardian of mitochondrial quality: Parkin function and Parkinson's disease. Transl Neurodegener *10*, 5. 10.1186/s40035-020-00229-8.

34.   Lois, C., Hong, E.J., Pease, S., Brown, E.J., and Baltimore, D. (2002). Germline transmission and tissue-specific expression of transgenes delivered by lentiviral vectors. Science *295*, 868-872. 10.1126/science.1067081.

35.   Schorpp, M., Jäger, R., Schellander, K., Schenkel, J., Wagner, E.F., Weiher, H., and Angel, P. (1996/05/01). The Human Ubiquitin C Promoter Directs High Ubiquitous Expression of Transgenes in Mice. Nucleic Acids Research *24*. 10.1093/nar/24.9.1787.

36.   Zufferey, R., Donello, J.E., Trono, D., and Hope, T.J. (1999/04). Woodchuck Hepatitis Virus Posttranscriptional Regulatory Element Enhances Expression of Transgenes Delivered by Retroviral Vectors. Journal of Virology *73*. 10.1128/jvi.73.4.2886-2892.1999.

37.   Higashimoto, T., Urbinati, F., Perumbeti, A., Jiang, G., Zarzuela, A., Chang, L.J., Kohn, D.B., and Malik, P. (2007). The woodchuck hepatitis virus post-transcriptional regulatory

882   element reduces readthrough transcription from retroviral vectors. Gene Therapy *14*,

883   1298-1304. 10.1038/sj.gt.3302979.

884   38.   Mosammaparast, N., Jackson, K.R., Guo, Y., Brame, C.J., Shabanowitz, J., Hunt, D.F.,

885   and Pemberton, L.F. (2001). Nuclear import of histone H2A and H2B is mediated by a

886   network of karyopherins. J Cell Biol *153*, 251-262. 10.1083/jcb.153.2.251.

887   39.   Marino-Ramirez, L., Kann, M.G., Shoemaker, B.A., and Landsman, D. (2005). Histone

888   structure and nucleosome stability. Expert Rev Proteomics *2*, 719-729.

889   10.1586/14789450.2.5.719.

890   40.   Smith, P.J., Wiltshire, M., and Errington, R.J. (2004). DRAQ5 labeling of nuclear DNA in

891   live and fixed cells. Curr Protoc Cytom *Chapter 7*, Unit 7 25.

892   10.1002/0471142956.cy0725s28.

893   41.   Zhitomirsky, B., Farber, H., and Assaraf, Y.G. (2018). LysoTracker and MitoTracker Red

894   are transport substrates of P-glycoprotein: implications for anticancer drug design

895   evading multidrug resistance. J Cell Mol Med *22*, 2131-2141. 10.1111/jcmm.13485.

896   42.   Chazotte, B. (2011). Labeling lysosomes in live cells with LysoTracker. Cold Spring Harb

897   Protoc *2011*, pdb prot5571. 10.1101/pdb.prot5571.

898   43.   Dang, Q., Zhou, H., Qian, J., Yang, L., Huang, J., Zhang, Y., and Shi, W. (2018). LAMP1

899   Overexpression Predicts for Poor Prognosis in Diffuse Large B-cell Lymphoma. Clin

900   Lymphoma Myeloma Leuk *18*, 749-754. 10.1016/j.clml.2018.07.288.

901   44.   Wang, Q.Q., Yao, J., Jin, Q., Wang, X.D., Zhu, H.J., Huang, F., Wang, W., Qiang, J.F.,

902   and Ni, Q.C. (2017). LAMP1 expression is associated with poor prognosis in breast

903   cancer. Oncol Lett *14*, 4729-4735. 10.3892/ol.2017.6757.

904   45.   Xu, Y., Cao, X., Zhang, S., Zhang, Y., and Shen, Z. (2017). High expression of LAMP1

905   as a prognostic marker in patients with epithelial ovarian cancer. Int J Clin Exp Pathol

906   *10*, 9104-9111.

907   46.   Ranjbar, M.A., and Jamshidi, M. (2022). Overexpression of Lysosome-Associated

908   Membrane Protein 1 in Oral Squamous Cell Carcinoma and its Correlation with Tumor

909   Differentiation and Metastasis. Iran J Otorhinolaryngol *34*, 3-8.

910   10.22038/IJORL.2021.51683.2772.

911   47.   Zong, S., Wu, M., Gu, J., Liu, T., Guo, R., and Yang, M. (2018). Structure of the intact

912   14-subunit human cytochrome c oxidase. Cell Res *28*, 1026-1034. 10.1038/s41422-018-

913   0071-1.

914   48.   Cunatova, K., Reguera, D.P., Houstek, J., Mracek, T., and Pecina, P. (2020). Role of

915   cytochrome c oxidase nuclear-encoded subunits in health and disease. Physiol Res *69*,

916   947-965. 10.33549/physiolres.934446.

917   49.   Partikian, A., Olveczky, B., Swaminathan, R., Li, Y., and Verkman, A.S. (1998). Rapid

918   diffusion of green fluorescent protein in the mitochondrial matrix. J Cell Biol *140*, 821-

919   829. 10.1083/jcb.140.4.821.

920   50.   Hoogewijs, K., James, A.M., Smith, R.A., Gait, M.J., Murphy, M.P., and Lightowlers, R.N.

921   (2016). Assessing the Delivery of Molecules to the Mitochondrial Matrix Using Click

922   Chemistry. Chembiochem *17*, 1312-1316. 10.1002/cbic.201600188.

923   51.   Candas, D., Qin, L., Fan, M., and Li, J.J. (2016). Experimental Approaches to Study

924   Mitochondrial Localization and Function of a Nuclear Cell Cycle Kinase, Cdk1. J Vis Exp,

925   53417. 10.3791/53417.

926   52.   Chazotte, B. (2011). Labeling mitochondria with MitoTracker dyes. Cold Spring Harb

927   Protoc *2011*, 990-992. 10.1101/pdb.prot5648.

928   53.   Durand, R.E., and Olive, P.L. (1982). Cytotoxicity, Mutagenicity and DNA damage by

929   Hoechst 33342. J Histochem Cytochem *30*, 111-116. 10.1177/30.2.7061816.

930   54.   Wiezorek, C. (1984). Cell cycle dependence of Hoechst 33342 dye cytotoxicity on sorted

931   living cells. Histochemistry *81*, 493-495. 10.1007/BF00489756.

932   55.   Solano, R.M., Casarejos, M.J., Menendez-Cuervo, J., Rodriguez-Navarro, J.A., Garcia

933   de Yebenes, J., and Mena, M.A. (2008). Glial dysfunction in parkin null mice: effects of

934   aging. J Neurosci *28*, 598-611. 10.1523/JNEUROSCI.4609-07.2008.

935   56.   Rouland, L., Duplan, E., Ramos Dos Santos, L., Bernardin, A., Katula, K.S., Manfioletti,

936   G., Idbaih, A., Checler, F., and Alves da Costa, C. (2021). Therapeutic potential of parkin

937   as a tumor suppressor via transcriptional control of cyclins in glioblastoma cell and

938   animal models. Theranostics *11*, 10047-10063. 10.7150/thno.57549.

939   57.   Wahabi, K., Perwez, A., and Rizvi, M.A. (2018). Parkin in Parkinson's Disease and

940   Cancer: a Double-Edged Sword. Mol Neurobiol *55*, 6788-6800. 10.1007/s12035-018-

941   0879-1.

942   58.   Yeo, C.W., Ng, F.S., Chai, C., Tan, J.M., Koh, G.R., Chong, Y.K., Koh, L.W., Foong, C.S.,

943   Sandanaraj, E., Holbrook, J.D., et al. (2012). Parkin pathway activation mitigates glioma

944   cell proliferation and predicts patient survival. Cancer Res *72*, 2543-2553. 10.1158/0008-

945   5472.CAN-11-3060.

946   59.   Tay, S.P., Yeo, C.W., Chai, C., Chua, P.J., Tan, H.M., Ang, A.X., Yip, D.L., Sung, J.X.,

947   Tan, P.H., Bay, B.H., et al. (2010). Parkin enhances the expression of cyclin-dependent

948   kinase 6 and negatively regulates the proliferation of breast cancer cells. J Biol Chem

949   *285*, 29231-29238. 10.1074/jbc.M110.108241.

950   60.   Gong, Y., Zack, T.I., Morris, L.G., Lin, K., Hukkelhoven, E., Raheja, R., Tan, I.L., Turcan,

951   S., Veeriah, S., Meng, S., et al. (2014). Pan-cancer genetic analysis identifies PARK2 as

952   a master regulator of G1/S cyclins. Nat Genet *46*, 588-594. 10.1038/ng.2981.

953   61.   Veeriah, S., Taylor, B.S., Meng, S., Fang, F., Yilmaz, E., Vivanco, I., Janakiraman, M.,

954   Schultz, N., Hanrahan, A.J., Pao, W., et al. (2010). Somatic mutations of the Parkinson's

955   disease-associated gene PARK2 in glioblastoma and other human malignancies. Nat

956   Genet *42*, 77-82. 10.1038/ng.491.

957 62. Frade, J.M., and Ovejero-Benito, M.C. (2015). Neuronal cell cycle: the neuron itself and
958   its circumstances. Cell Cycle *14*, 712-720. 10.1080/15384101.2015.1004937.

959 63. Kruman, II, Wersto, R.P., Cardozo-Pelaez, F., Smilenov, L., Chan, S.L., Chrest, F.J.,
960   Emokpae, R., Jr., Gorospe, M., and Mattson, M.P. (2004). Cell cycle activation linked to
961   neuronal cell death initiated by DNA damage. Neuron *41*, 549-561. 10.1016/s0896-
962   6273(04)00017-0.

963 64. Gupta, R., Jha, A., Ambasta, R.K., and Kumar, P. (2021). Regulatory mechanism of
964   cyclins and cyclin-dependent kinases in post-mitotic neuronal cell division. Life Sci *285*,
965   120006. 10.1016/j.lfs.2021.120006.

966 65. Gan-Or, Z., Dion, P.A., and Rouleau, G.A. (2015). Genetic perspective on the role of the
967   autophagy-lysosome pathway in Parkinson disease. Autophagy *11*, 1443-1457.
968   10.1080/15548627.2015.1067364.

969 66. Navarro-Romero, A., Montpeyo, M., and Martinez-Vicente, M. (2020). The Emerging
970   Role of the Lysosome in Parkinson's Disease. Cells *9*. 10.3390/cells9112399.

971 67. Hopfner, F., Mueller, S.H., Szymczak, S., Junge, O., Tittmann, L., May, S., Lohmann, K.,
972   Grallert, H., Lieb, W., Strauch, K., et al. (2020). Rare Variants in Specific Lysosomal
973   Genes Are Associated With Parkinson's Disease. Mov Disord *35*, 1245-1248.
974   10.1002/mds.28037.

975 68. Dehay, B., Martinez-Vicente, M., Caldwell, G.A., Caldwell, K.A., Yue, Z., Cookson, M.R.,
976   Klein, C., Vila, M., and Bezard, E. (2013). Lysosomal impairment in Parkinson's disease.
977   Mov Disord *28*, 725-732. 10.1002/mds.25462.

978 69. Klein, A.D., and Mazzulli, J.R. (2018). Is Parkinson's disease a lysosomal disorder?
979   Brain *141*, 2255-2262. 10.1093/brain/awy147.

980 70. Yoshimori, T., Yamamoto, A., Moriyama, Y., Futai, M., and Tashiro, Y. (1991). Bafilomycin
981   A1, a specific inhibitor of vacuolar-type H(+)-ATPase, inhibits acidification and protein
982   degradation in lysosomes of cultured cells. J Biol Chem *266*, 17707-17712.

983 71. Mauvezin, C., and Neufeld, T.P. (2015). Bafilomycin A1 disrupts autophagic flux by inhibiting both V-ATPase-dependent acidification and Ca-P60A/SERCA-dependent autophagosome-lysosome fusion. Autophagy *11*, 1437-1438. 10.1080/15548627.2015.1066957.

987 72. Carpenter, A.E., Jones, T.R., Lamprecht, M.R., Clarke, C., Kang, I.H., Friman, O., Guertin, D.A., Chang, J.H., Lindquist, R.A., Moffat, J., et al. (2006). CellProfiler: image analysis software for identifying and quantifying cell phenotypes. Genome Biol *7*, R100. 10.1186/gb-2006-7-10-r100.

991 73. Johnson, D.E., Ostrowski, P., Jaumouille, V., and Grinstein, S. (2016). The position of lysosomes within the cell determines their luminal pH. J Cell Biol *212*, 677-692. 10.1083/jcb.201507112.

994 74. Heuser, J. (1989). Changes in lysosome shape and distribution correlated with changes in cytoplasmic pH. J Cell Biol *108*, 855-864. 10.1083/jcb.108.3.855.

996 75. Parton, R.G., Dotti, C.G., Bacallao, R., Kurtz, I., Simons, K., and Prydz, K. (1991). pH-induced microtubule-dependent redistribution of late endosomes in neuronal and epithelial cells. J Cell Biol *113*, 261-274. 10.1083/jcb.113.2.261.

999 76. Pu, J., Guardia, C.M., Keren-Kaplan, T., and Bonifacino, J.S. (2016). Mechanisms and functions of lysosome positioning. J Cell Sci *129*, 4329-4339. 10.1242/jcs.196287.

1001 77. Song, P., Trajkovic, K., Tsunemi, T., and Krainc, D. (2016). Parkin Modulates Endosomal Organization and Function of the Endo-Lysosomal Pathway. J Neurosci *36*, 2425-2437. 10.1523/JNEUROSCI.2569-15.2016.

1004 78. Okarmus, J., Bogetofte, H., Schmidt, S.I., Ryding, M., Garcia-Lopez, S., Ryan, B.J., Martinez-Serrano, A., Hyttel, P., and Meyer, M. (2020). Lysosomal perturbations in human dopaminergic neurons derived from induced pluripotent stem cells with PARK2 mutation. Sci Rep *10*, 10278. 10.1038/s41598-020-67091-6.

79. Twig, G., Elorza, A., Molina, A.J., Mohamed, H., Wikstrom, J.D., Walzer, G., Stiles, L., Haigh, S.E., Katz, S., Las, G., et al. (2008). Fission and selective fusion govern mitochondrial segregation and elimination by autophagy. EMBO J *27*, 433-446. 10.1038/sj.emboj.7601963.

80. Chen, H., Chomyn, A., and Chan, D.C. (2005). Disruption of fusion results in mitochondrial heterogeneity and dysfunction. J Biol Chem *280*, 26185-26192. 10.1074/jbc.M503062200.

81. Sarrafha, L., Parfitt, G.M., Reyes, R., Goldman, C., Coccia, E., Kareva, T., and Ahfeldt, T. (2021). High-throughput generation of midbrain dopaminergic neuron organoids from reporter human pluripotent stem cells. STAR Protoc *2*, 100463. 10.1016/j.xpro.2021.100463.

82. Wang, X., Winter, D., Ashrafi, G., Schlehe, J., Wong, Y.L., Selkoe, D., Rice, S., Steen, J., LaVoie, M.J., and Schwarz, T.L. (2011). PINK1 and Parkin target Miro for phosphorylation and degradation to arrest mitochondrial motility. Cell *147*, 893-906. 10.1016/j.cell.2011.10.018.

83. Hernandez, G., Thornton, C., Stotland, A., Lui, D., Sin, J., Ramil, J., Magee, N., Andres, A., Quarato, G., Carreira, R.S., et al. (2013). MitoTimer: a novel tool for monitoring mitochondrial turnover. Autophagy *9*, 1852-1861. 10.4161/auto.26501.

84. Laker, R.C., Xu, P., Ryall, K.A., Sujkowski, A., Kenwood, B.M., Chain, K.H., Zhang, M., Royal, M.A., Hoehn, K.L., Driscoll, M., et al. (2014). A novel MitoTimer reporter gene for mitochondrial content, structure, stress, and damage in vivo. J Biol Chem *289*, 12005-12015. 10.1074/jbc.M113.530527.

85. Hanson, G.T., Aggeler, R., Oglesbee, D., Cannon, M., Capaldi, R.A., Tsien, R.Y., and Remington, S.J. (2004). Investigating mitochondrial redox potential with redox-sensitive green fluorescent protein indicators. J Biol Chem *279*, 13044-13053. 10.1074/jbc.M312846200.

86. Yokomakura, A., Hong, J., Ohuchi, K., Oh, S.E., Lee, J.Y., Mano, N., Takahashi, T., Hwang, G.W., and Naganuma, A. (2012). Increased production of reactive oxygen species by the vacuolar-type (H(+))-ATPase inhibitors bafilomycin A1 and concanamycin A in RAW 264 cells. J Toxicol Sci *37*, 1045-1048. 10.2131/jts.37.1045.

87. Palacino, J.J., Sagi, D., Goldberg, M.S., Krauss, S., Motz, C., Wacker, M., Klose, J., and Shen, J. (2004). Mitochondrial dysfunction and oxidative damage in parkin-deficient mice. J Biol Chem *279*, 18614-18622. 10.1074/jbc.M401135200.

88. Cornejo-Olivas, M.R., Torres, L., Mata, I.F., Mazzetti, P., Rivas, D., Cosentino, C., Inca-Martinez, M., Cuba, J.M., Zabetian, C.P., and Leverenz, J.B. (2015). A Peruvian family with a novel PARK2 mutation: Clinical and pathological characteristics. Parkinsonism Relat Disord *21*, 444-448. 10.1016/j.parkreldis.2015.01.005.

89. Orimo, S., Amino, T., Yokochi, M., Kojo, T., Uchihara, T., Takahashi, A., Wakabayashi, K., Takahashi, H., Hattori, N., and Mizuno, Y. (2005). Preserved cardiac sympathetic nerve accounts for normal cardiac uptake of MIBG in PARK2. Mov Disord *20*, 1350-1353. 10.1002/mds.20594.

90. Gouider-Khouja, N., Larnaout, A., Amouri, R., Sfar, S., Belal, S., Ben Hamida, C., Ben Hamida, M., Hattori, N., Mizuno, Y., and Hentati, F. (2003). Autosomal recessive parkinsonism linked to parkin gene in a Tunisian family. Clinical, genetic and pathological study. Parkinsonism Relat Disord *9*, 247-251. 10.1016/s1353-8020(03)00016-6.

91. Hayashi, S., Wakabayashi, K., Ishikawa, A., Nagai, H., Saito, M., Maruyama, M., Takahashi, T., Ozawa, T., Tsuji, S., and Takahashi, H. (2000). An autopsy case of autosomal-recessive juvenile parkinsonism with a homozygous exon 4 deletion in the parkin gene. Mov Disord *15*, 884-888. 10.1002/1531-8257(200009)15:5<884::aid-mds1019>3.0.co;2-8.

92. Schmidt, S., Linnartz, B., Mendritzki, S., Sczepan, T., Lubbert, M., Stichel, C.C., and Lubbert, H. (2011). Genetic mouse models for Parkinson's disease display severe

1060   pathology in glial cell mitochondria. Hum Mol Genet *20*, 1197-1211.

1061   10.1093/hmg/ddq564.

1062 93. Gerasimova, T., Stepanenko, E., Novosadova, L., Arsenyeva, E., Shimchenko, D.,

1063   Tarantul, V., Grivennikov, I., Nenasheva, V., and Novosadova, E. (2023). Glial Cultures

1064   Differentiated from iPSCs of Patients with PARK2-Associated Parkinson's Disease

1065   Demonstrate a Pro-Inflammatory Shift and Reduced Response to TNFalpha Stimulation.

1066   Int J Mol Sci *24*. 10.3390/ijms24032000.

1067 94. Hastie, E., Cataldi, M., Marriott, I., and Grdzelishvili, V.Z. (2013). Understanding and

1068   altering cell tropism of vesicular stomatitis virus. Virus Res *176*, 16-32.

1069   10.1016/j.virusres.2013.06.003.

1070 95. Sweeney, N.P., and Vink, C.A. (2021). The impact of lentiviral vector genome size and

1071   producer cell genomic to gag-pol mRNA ratios on packaging efficiency and titre. Mol

1072   Ther Methods Clin Dev *21*, 574-584. 10.1016/j.omtm.2021.04.007.

1073 96. Desfarges, S., and Ciuffi, A. (2010). Retroviral integration site selection. Viruses *2*, 111-

1074   130. 10.3390/v2010111.

1075 97. Bonam, S.R., Wang, F., and Muller, S. (2019). Lysosomes as a therapeutic target. Nat

1076   Rev Drug Discov *18*, 923-948. 10.1038/s41573-019-0036-1.

1077 98. Zhang, Z., Yue, P., Lu, T., Wang, Y., Wei, Y., and Wei, X. (2021). Role of lysosomes in

1078   physiological activities, diseases, and therapy. J Hematol Oncol *14*, 79. 10.1186/s13045-

1079   021-01087-1.

1080 99. Javadov, S., Kozlov, A.V., and Camara, A.K.S. (2020). Mitochondria in Health and

1081   Diseases. Cells *9*. 10.3390/cells9051177.

1082 100. Chen, W., Zhao, H., and Li, Y. (2023). Mitochondrial dynamics in health and disease:

1083   mechanisms and potential targets. Signal Transduct Target Ther *8*, 333.

1084   10.1038/s41392-023-01547-9.

1085   101.   Dull, T., Zufferey, R., Kelly, M., Mandel, R.J., Nguyen, M., Trono, D., and Naldini, L.

1086   (1998). A third-generation lentivirus vector with a conditional packaging system. J Virol

1087   *72*, 8463-8471. 10.1128/JVI.72.11.8463-8471.1998.

1088   102.   Morrone Parfitt, G., Coccia, E., Goldman, C., Whitney, K., Reyes, R., Sarrafha, L., Nam,

1089   K.H., Sohail, S., Jones, D.R., Crary, J.F., et al. (2024). Disruption of lysosomal

1090   proteolysis in astrocytes facilitates midbrain organoid proteostasis failure in an early-

1091   onset Parkinson's disease model. Nat Commun *15*, 447. 10.1038/s41467-024-44732-2.

1092   103.   Chaudhry, A., Shi, R., and Luciani, D.S. (2020). A pipeline for multidimensional confocal

1093   analysis of mitochondrial morphology, function, and dynamics in pancreatic beta-cells.

1094   Am J Physiol Endocrinol Metab *318*, E87-E101. 10.1152/ajpendo.00457.2019.

1095   104.   Mangeol, P., Prevo, B., and Peterman, E.J. (2016). KymographClear and

1096   KymographDirect: two tools for the automated quantitative analysis of molecular and

1097   cellular dynamics using kymographs. Mol Biol Cell *27*, 1948-1957. 10.1091/mbc.E15-06-

1098   0404.

1099   105.   Stirling, D.R., Swain-Bowden, M.J., Lucas, A.M., Carpenter, A.E., Cimini, B.A., and

1100   Goodman, A. (2021). CellProfiler 4: improvements in speed, utility and usability. BMC
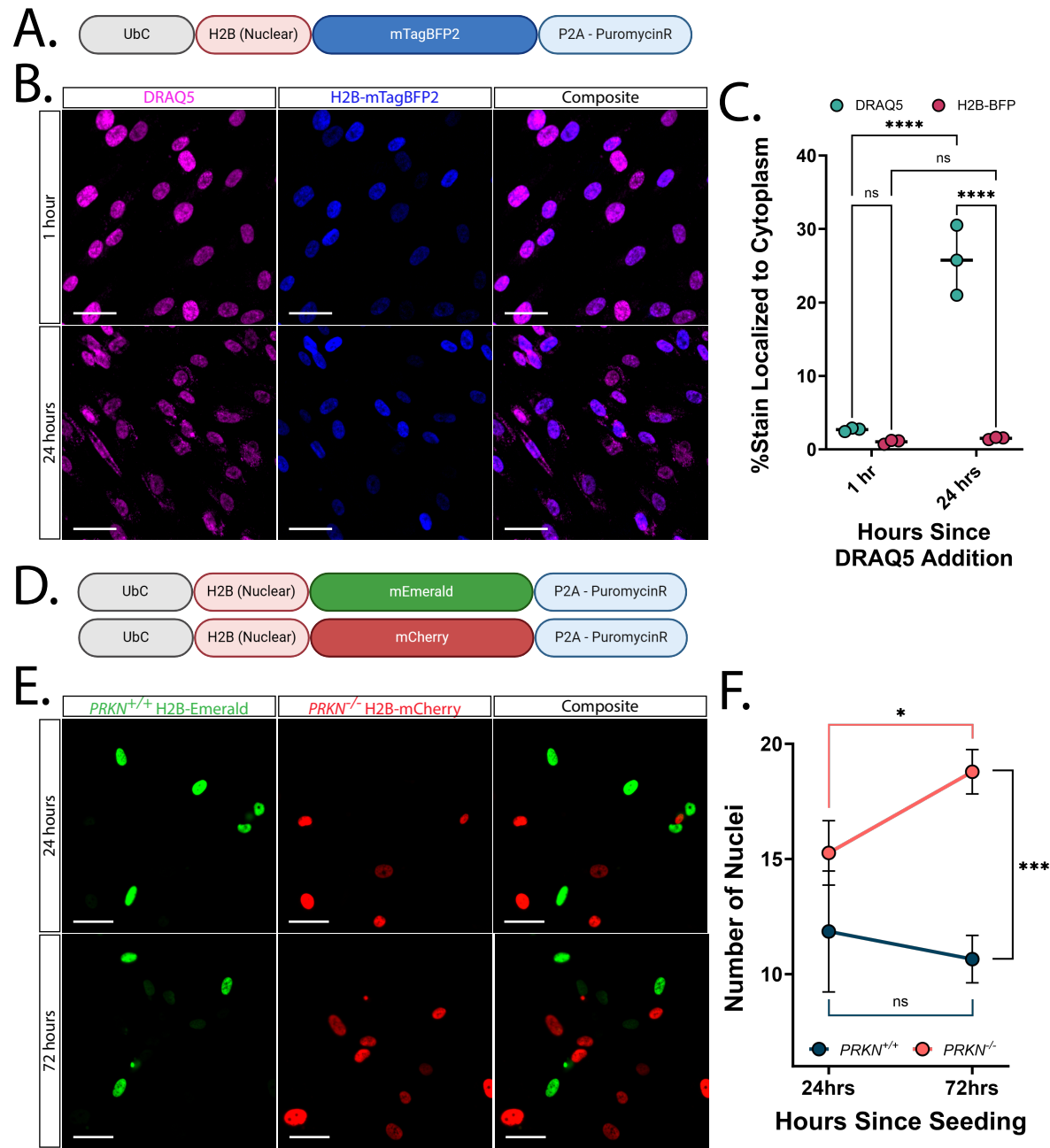
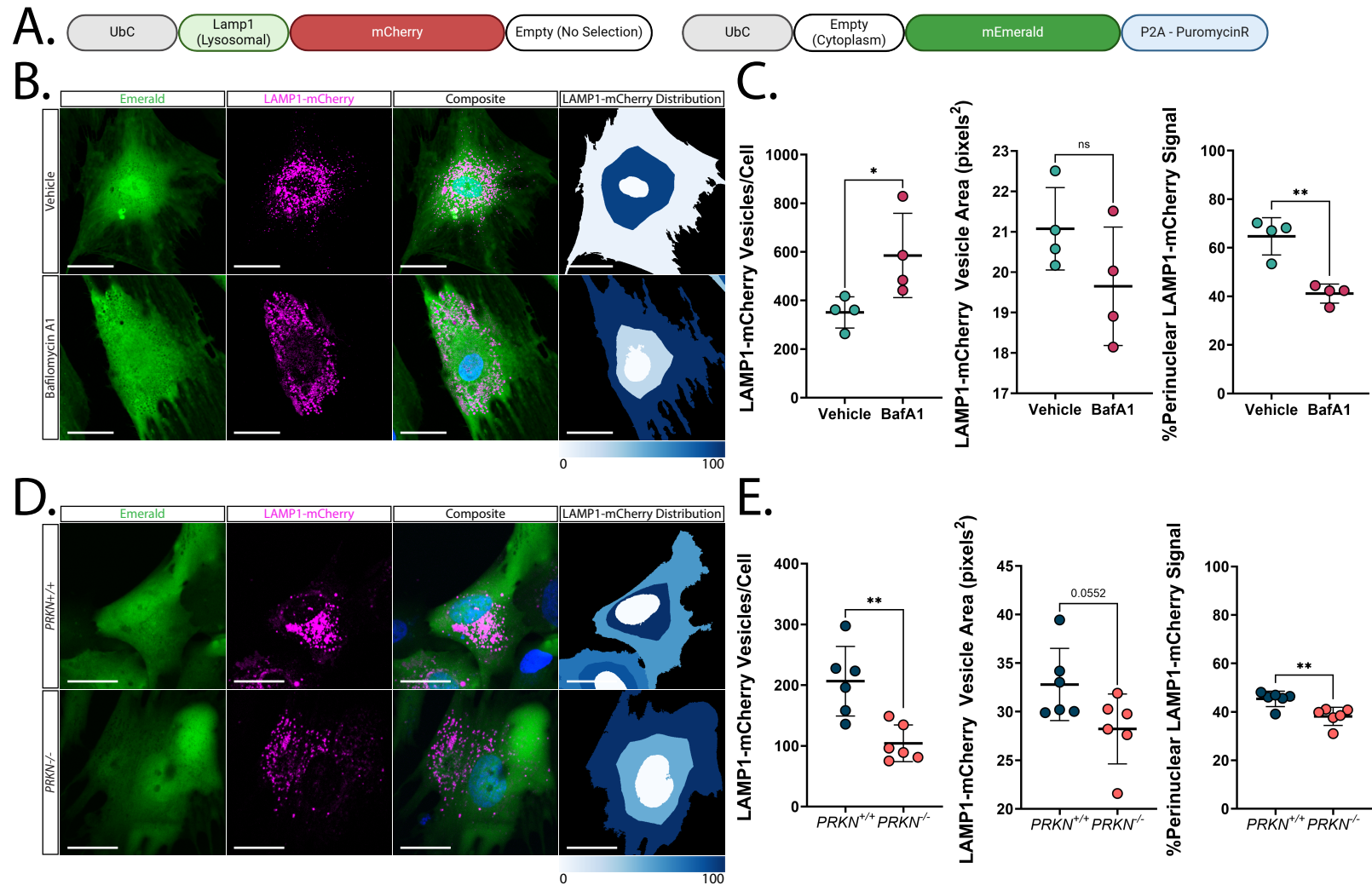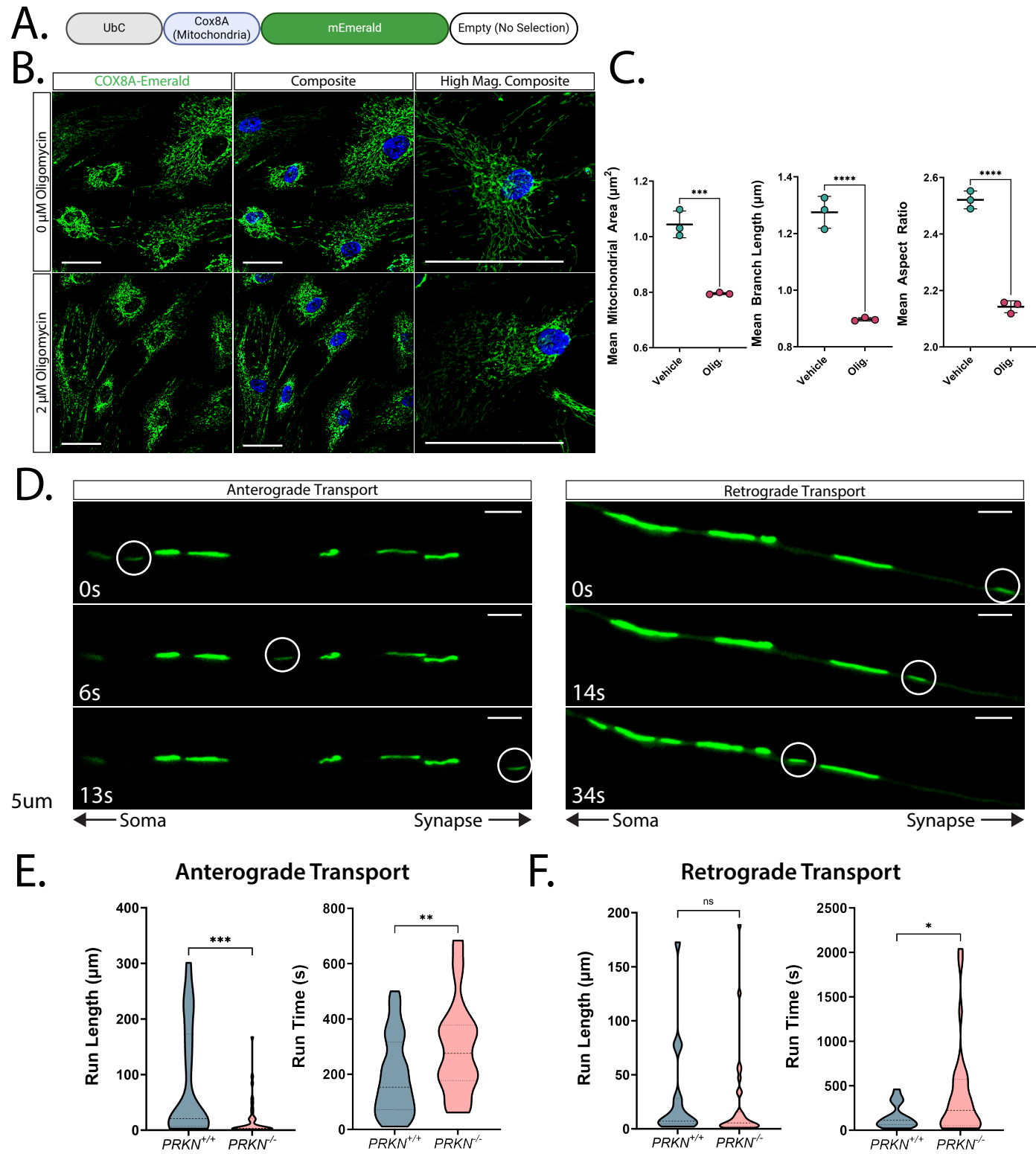1101   Bioinformatics *22*, 433. 10.1186/s12859-021-04344-9.
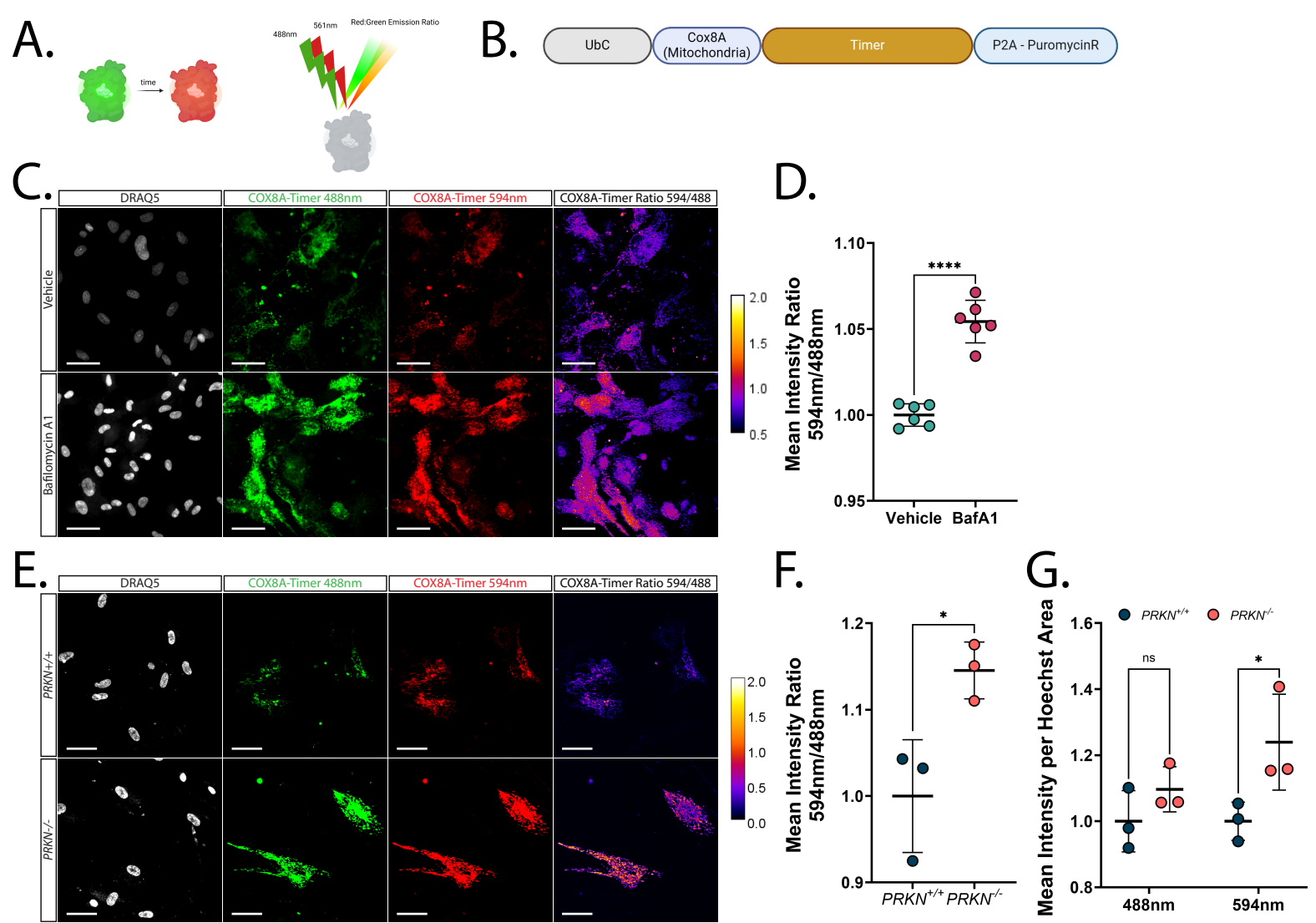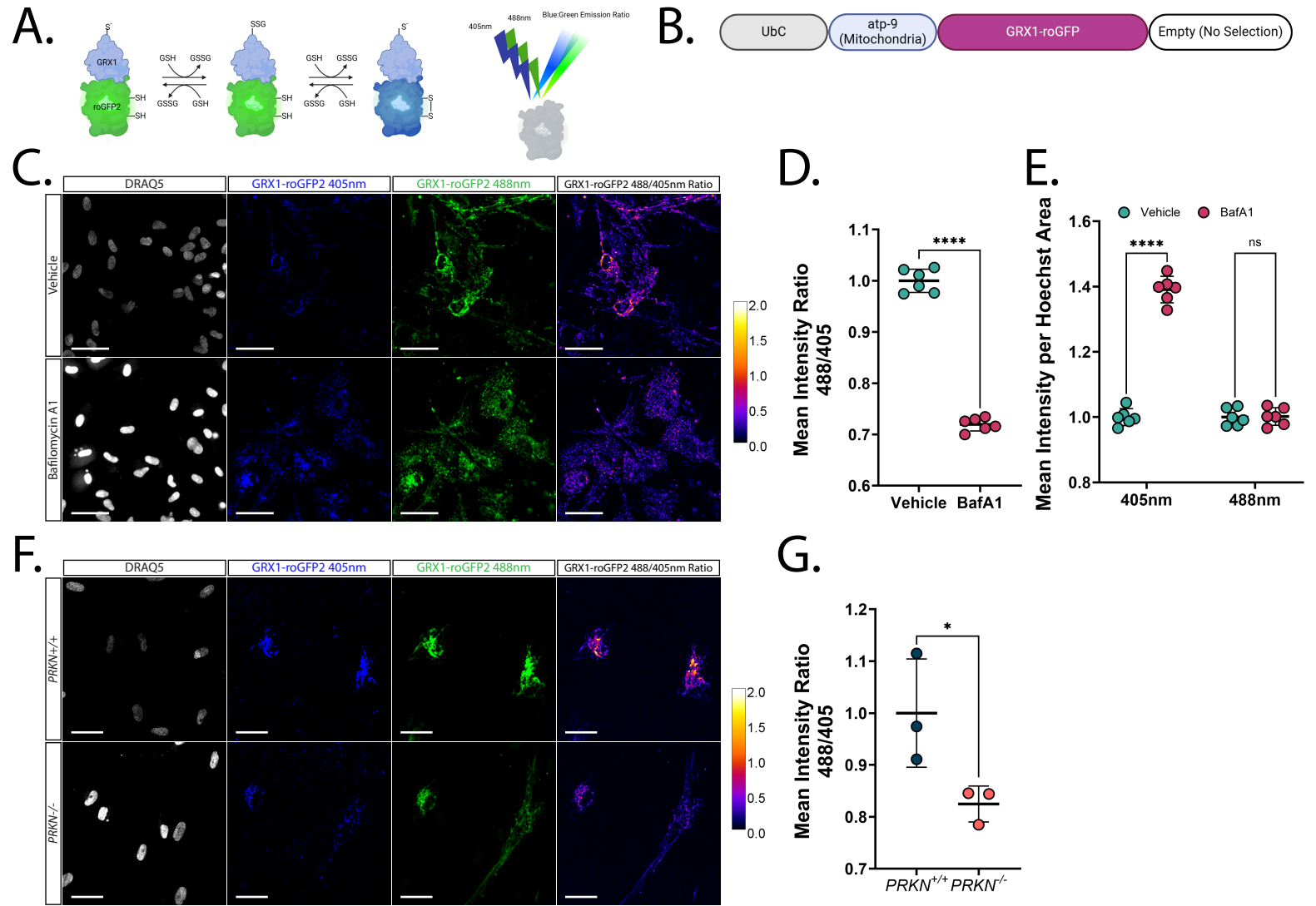
1102

Figure 1
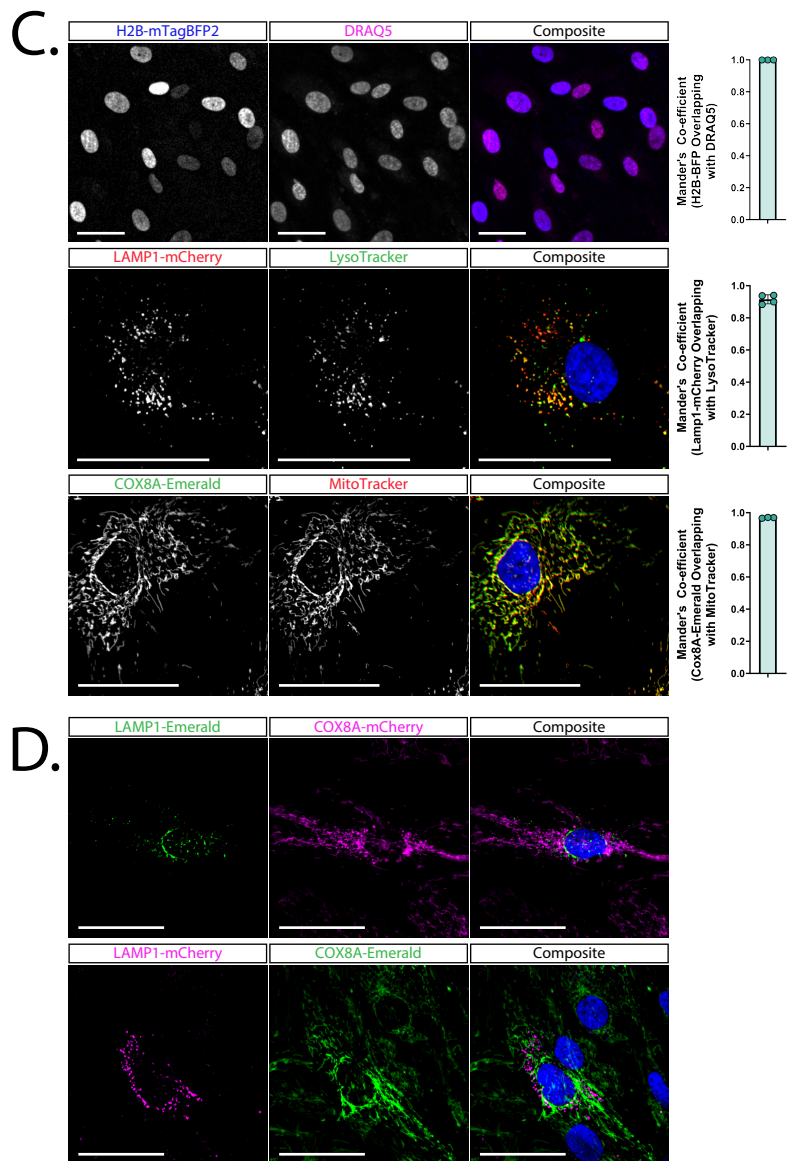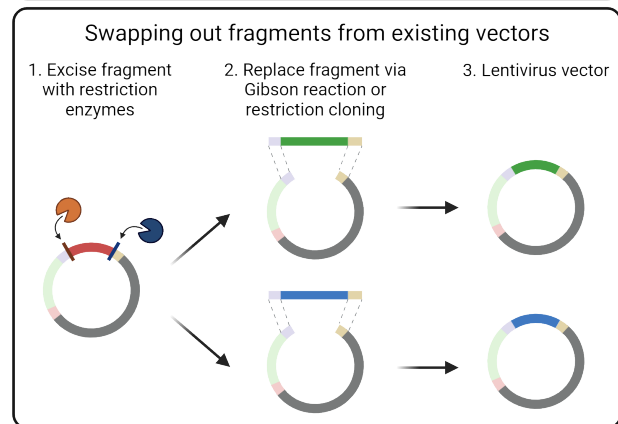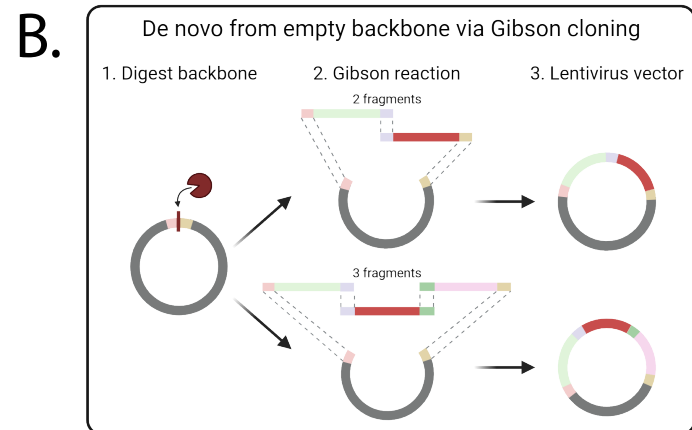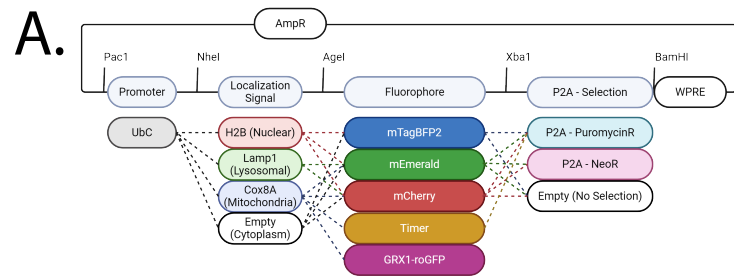
Figure 2
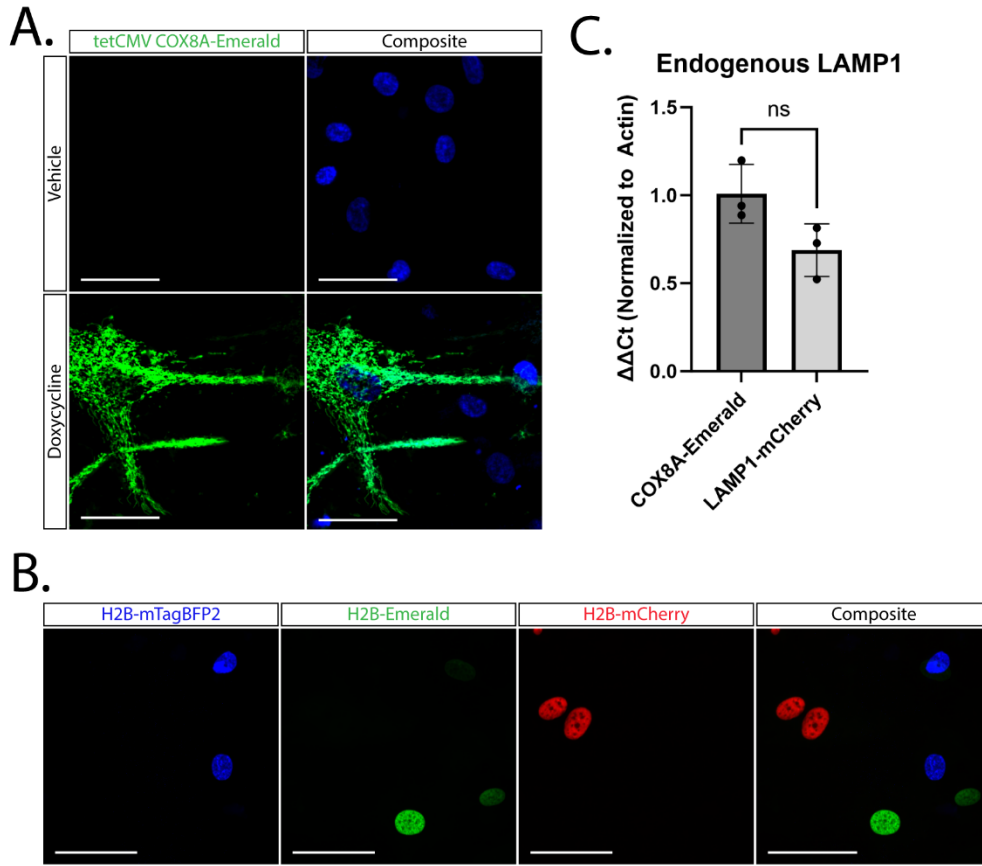
# Figure 3

Figure 4

Figure 5

Figure 6

Figure S1

Fig. S1: GEM-SCOPe supports a diversity of modifications and applications (A) Representative images of astrocytes expressing COX8A-Emerald under the control of a doxycycline inducible promoter. Astrocytes were treated with a vehicle (DMSO; top) or doxycycline (bottom) for 72 hours. Nuclei were stained with Hoechst33342. **(B)** qPCR for endogenous *LAMP1* on RNA from astrocytes transduced with a virus localized to the lysosome (LAMP1-mCherry) or a virus not localized to the lysosome (COX8A-Emerald). qPCR primers were designed to amplify a sequence of *LAMP1* that is not included in the lentivirus to only quantify endogenous *LAMP1* levels. Bars represent mean and error bars represent standard deviation (n = 3 independent transductions). **(C)** Representative images of a mixed population of astrocytes with nuclei expressing different H2B-fusion fluorophores. Astrocytes were transduced with a single lentivirus and then plated together. Scale bar = 50 μm.

Figure S2
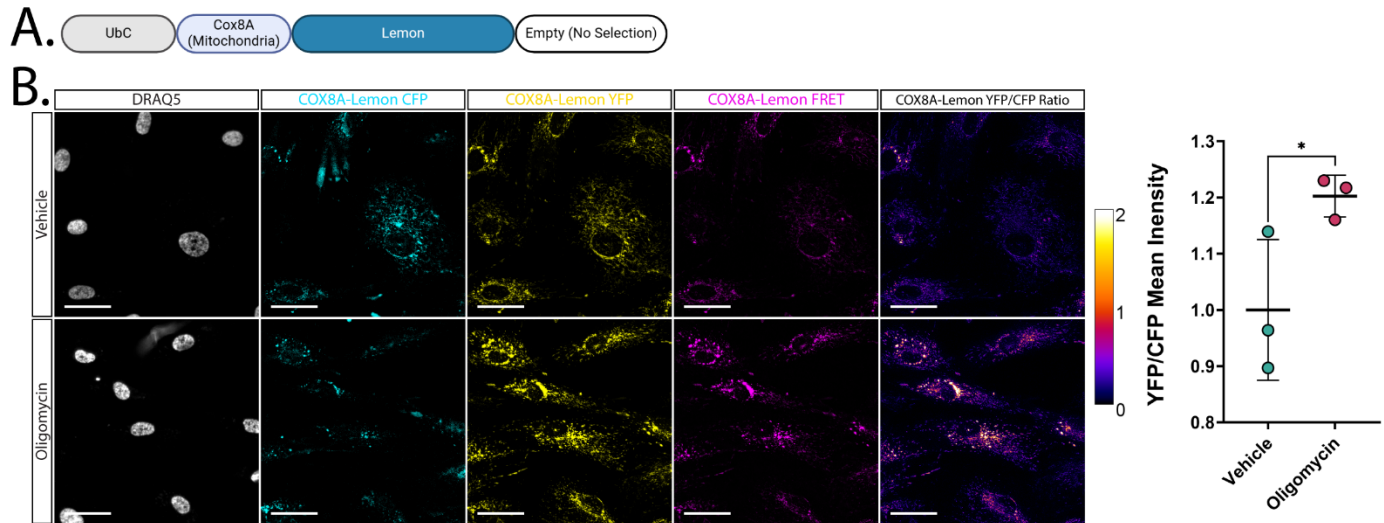
Fig. S2: Mitochondrial pH sensor measures disrupted mitochondrial membrane potential Schematic of the lentiviral construct used in the following panels localizing Lemon, a pH responsive fluorophore, to the mitochondria with the targeting sequence of COX8A. Lemon undergoes Forster Resonance Energy Transfer (FRET) under alkaline conditions. **(B)** Representative images of astrocytes transduced with COX8A-Lemon and treated with a vehicle (DMSO; top) or 2 μM oligomycin (bottom) for 24 hours. Images were acquired with a 455nm-excitation laser and a 515-excitation laser. Far right: ratiometric representation of the emission in the yellow channel divided by the emission in the cyan channel and then pseudo colored so that orange, yellow and white indicate more relative yellow emission (more alkaline) while black and purple represent more cyan emission (more acidic). Nuclei were stained with DRAQ5. Scale bars = 50 μm. **(C)** Quantification of the ratio of yellow emission to cyan emission in astrocytes expressing COX8A-Lemon and treated with DMSO or oligomycin. Central bars represent mean and error bars represent standard deviation (n = 3; each replicate is an average 36 images).

Figure S3
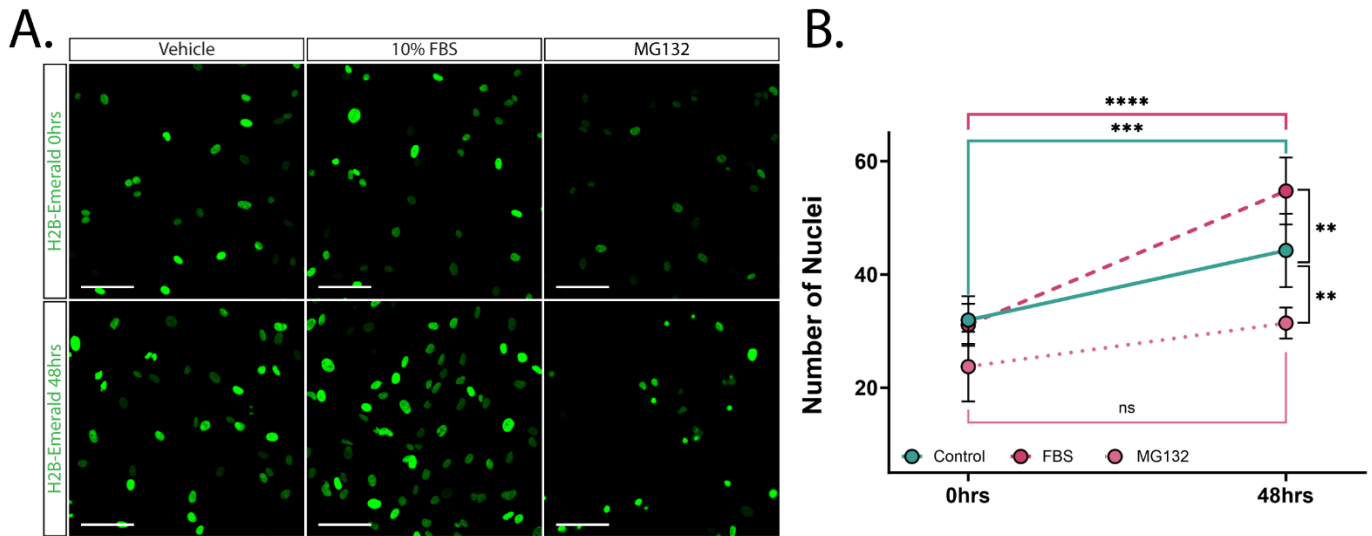
Fig. S3: Astrocyte proliferation is activated by FBS and inhibited by MG-132 (A) Representative images of astrocytes transduced with H2B-Emerald lentivirus after 0 hrs (top) or 48 hrs (bottom) of treatment with a vehicle (DMSO; left), 10% fetal bovine serum (FBS; middle), or MG132 (right). Scale bars = 50 μm. **(B)** Quantification of number of H2B-Emerald nuclei per image field 0 hours and 48 hours after treatment. Dots represent mean values and error bars represent standard deviation (n = 6 (n = 3 for MG-132 treatment) per time point; each replicate is an average over 25 images). Scale bars = 50 μm. All images were acquired on the CX7 HCS platform with a 20x objective lens.

Figure S4
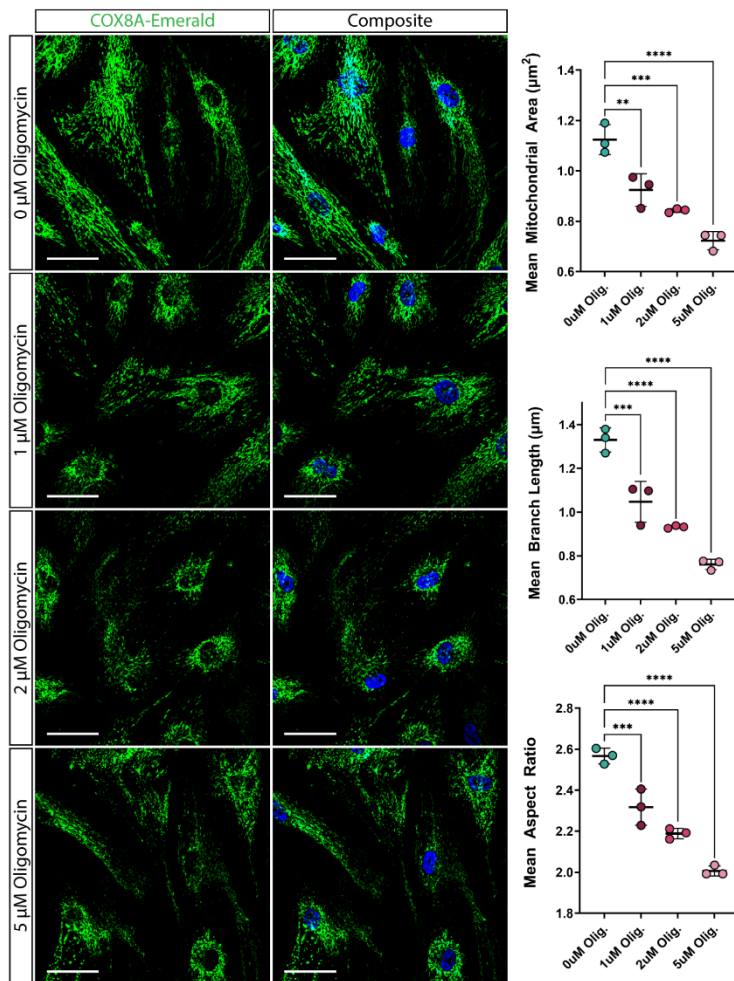
Fig. S4: Mitochondrial fragmentation exhibits a dose dependent response to oligomycin-induced stress

(A) Representative images of astrocytes transduced with COX8A-Emerald and treated with a vehicle (DMSO), 1μM, 2 μM, or 5 μM oligomycin for 4 hours. Nuclei were stained with Hoechst33342. Scale bars = 50 μm **(B)** Quantification of mitochondrial features indicative of mitochondrial network fragmentation: mean area, perimeter, aspect ratio, number of branches, branch length, and number of branch endpoints. Central bars represent mean and error bars represent standard deviation (n = 3; each replicate is an average over 36 images).

Plasmid Name	AddGene Cat#	Localization	Fluorophore	Antibiotic Resistance	Relevant Figures
pFUW H2B-mTagBFP2-p2A-PuroR		Nucleus	mTagBFP2	Puromycin	1, 2, S1, S3
pFUW H2B-Emerald-p2A-PuroR		Nucleus	Emerald	Puromycin	2, S1
pFUW H2B-mCherry-p2A-PuroR		Nucleus	mCherry	Puromycin	2, S1
pFUW LAMP1Sig-Emerald		Lysosome	Emerald	NA	1, 3
pFUW LAMP1Sig-mCherry		Lysosome	mCherry	NA	1
pFUW COX8ASig-Emerald		Mitochondria	Emerald	NA	1, 4, S5
pFUW COX8ASig-mCherry		Mitochondria	mCherry	NA	1
pFUW PuroR-P2A-COX8ASig-Timer		Mitochondria	Timer	Puromycin	5
pFUW COX8ASig-Lemon		Mitochondria	Lemon	NA	S2
pFUW mito-GRX1-roGFP2		Mitochondria	roGFP2	NA	6
pFUW mTagBFP2		NA	mTagBFP2	NA	NA
pFUW Emerald		NA	Emerald	NA	NA
pFUW mCherry		NA	mCherry	NA	NA
pFUW mTagBFP2-P2A-PuroR		NA	mTagBFP2	Puromycin	NA
pFUW Emerald-P2A-PuroR		NA	Emerald	Puromycin	3
pFUW mCherry-P2A-PuroR		NA	mCherry	Puromycin	NA
pFUW mTagBFP2-P2A-NeoR		NA	mTagBFP2	Neomycin	NA
pFUW Emerald-P2A-NeoR		NA	Emerald	Neomycin	NA
pFUW mCherry-P2A-NeoR		NA	mCherry	Neomycin	NA

Table S1: A list of all plasmids generated in this study. Details for all plasmids, including subcellular localization, fluorophore, antibiotic resistance, and in which figure each plasmid was used. More plasmids were generated as part of GEM-SCOPe than used in the final publication, and these are also included here and available on Addgene.

Video S1: Mitochondrial axonal transport in *PRKN*$^{+/+}$ and *PRKN*$^{-/-}$ human iPSC derived neurons

Representative videos of COX8A-Emerald labeled mitochondria moving within neuronal axons over the course of 1 hour. Images were taken every 10 seconds and sped up 70x. Scale bar = 25 µm.